KTH Royal Institute of Technology
and
Universitat Politècnica de Catalunya

Master Thesis

Water Drop Lens Antenna for sub-THz Imaging

Author:
Joan Mitjans

Supervisor:
Pilar Castillo (KTH)
Jordi Romeu (UPC)

Examiner:
Oscar Quevedo (KTH)

Stockholm, Sweden
July 6, 2021

Abstract

The Millimiter Wave (mmW) frequency band, characterized by a high atmospheric attenuation and wide available bandwidth has become of big interest for high accuracy radar imaging applications. The continuous development of the Monolithic Microwave Integrated Circuit (MMIC) technology yields to the appearance of different commercial-off-the-shelf (COTS) radar transceivers at that frequency band, where the antennas are fully integrated into the chip.

Lenses are being used to correct the phase front of those MMIC improving the directivity and therefore the operating range. Fully metallic geodesic lenses offer the attractive properties of common dielectric lenses without their material losses.

In this master thesis, a specific water-drop geodesic lens antenna with focusing properties has been designed to enhance the radar imaging capabilities of the *TRA-120-002* transceiver working at the 120 GHz Industrial, Scientific and Medical (ISM) band.

Different transitions for the antenna singular points have been studied to minimize reflections without increasing aberrations in the lens. An optimized design of a radiating flare is shown where corrugations are used to improve the antenna radiation pattern. A small feeding horn antenna with a bed-of-nails Electromagnetic Band-Gap (EBG) metasurface has been designed to maximize the energy transmission between the COTS transceiver and the lens. Finally, a glide-symmetric holey metasurface has been added to prevent leakage between the antenna plates due to manufacturing limitations.

The results show that a fully metallic folded lens antenna with 5λ radius can achieve directivities higher than 19.5 dB and side-lobe levels (SLL) between -10.5 dB and -9.2 dB within the 119 GHz - 125.5 GHz band while having an image point located at 30 cm from the antenna.

Sammanfattning

Frekvensbandet för millimetervågor (mmW), som kännetecknas av en hög atmosfärisk dämpning och stor tillgänglig bandbredd har blivit av stort intresse för tillämpningar med hög noggrannhet för radarbild. Den kontinuerliga utvecklingen av monolitisk mikrovågsintegrerad kretsteknologi (MMIC) ger upphov till olika kommersiella lösningar (COTS) för radarsändtagare vid det frekvensband där antennerna är helt integrerade i chipet.

Linser används för att korrigera fasfronten hos de MMIC som förbättrar riktningen och därmed driftsområdet. Helt metalliska geodetiska linser erbjuder de eftertraktade egenskaperna hos vanliga dielektriska linser utan att det uppstår materiella förluster.

I det här examensarbetet har en specifik geodetisk linsantenn i form av en vattendroppe med fokuseringsegenskaper utformats för att förbättra radaravbildningsfunktionerna hos TRA-120-002 sändtagare som arbetar med 120 GHz ISM band.

Olika övergångar för antennens enstaka punkter har studerats för att minimera reflektioner utan att samtidigt öka avvikelser i linsen. En optimerad design av ett strålningsflare visas där korrugeringar används för att förbättra antennens strålningsmönster. En liten hornantenn med en elektromagnetisk bandgapsmetayta (EBG) har utformats för att maximera energiöverföringen mellan COTS-sändtagaren och linsen. Slutligen har en glidsymmetrisk och hålformig metayta lagts till för att förhindra läckage mellan antennplattorna på grund av tillverkningsbegränsningar.

Resultaten visar att en helt metallisk, vikt linsantenn med 5λ radie kan uppnå en högre direktivitet än 19,5 dB med sidolobnivåer (SLL) mellan -10,5 dB och -9,2 dB. Detta kan uppnås inom bandet 119 GHz - 125,5 GHz när en bildpunkt ligger 30 cm från antennen.

Resum

La banda de freqüències d'ones mil·limètriques (mmW), caracteritzada per una elevada atenuació atmosfèrica i un gran ample de banda disponible, ha esdevingut de gran interès per a aplicacions d'imatges de radar d'alta precisió. El desenvolupament continu de la tecnologia de circuits de microones monolítics integrats (MMIC) dona lloc a l'aparició de diferents transceptors de radar comercials (COTS) en aquesta banda de freqüència, on les antenes estan totalment integrades al xip per evitar pèrdues en el substrat.

Les lents s'utilitzen per corregir el front de fase d'aquests xips millorant la directivitat i, per tant, el rang de funcionament. Les lents geodèsiques, que poden ser construïdes utilitzant només metalls, ofereixen les propietats atractives de les lents dielèctriques comuns sense les seves pèrdues en el material.

En aquest treball de fi de màster s'ha dissenyat una antena del tipus lent geodèsica específica amb propietats d'enfocament per millorar les capacitats d'imatge de radar del transceptor TRA-120-002 que treballa a la banda ISM de 120 GHz.

S'ha fet un estudi de diferents transicions per als punts singulars de l'antena, minimitzant reflexions sense augmentar les aberracions a la lent. En el treball es mostra un disseny optimitzat de l'obertura de la antena on s'utilitzen corrugacions per millorar el diagrama de radiació. S'ha dissenyat també una petita antena d'obertura amb una metasuperfície de pins periòdics per maximitzar la transmissió d'energia entre el transceptor COTS i la lent. Finalment, s'ha afegit una metasuperfície basada en forats amb simetria lliscada per evitar pèrdues entre les plaques de l'antena a causa de possibles limitacions en la seva fabricació.

Els resultats mostren que es pot aconseguir una antena de tipus lent de 5λ de radi totalment metàl·lica amb directivitat superior a 19,5 dB i nivells de lòbuls secundaris (SLL) entre -10,5 dB i -9,2 dB dins de la banda de 119 GHz - 125,5 GHz mentre que l'antena focalitza a 30 cm.

Resumen

La banda de frecuencias de ondas milimétricas (MMW), caracterizada por una elevada atenuación atmosférica y un gran ancho de banda disponible, se ha convertido de gran interés para aplicaciones de imágenes de radar de alta precisión. El desarrollo continuo de la tecnología de circuitos de microondas monolíticos integrados (MMIC) da lugar a la aparición de diferentes transceptores de radar comerciales (COTS) en esta banda de frecuencia, donde las antenas están totalmente integradas en el chip para evitar pérdidas en el sustrato.

Las lentes se utilizan para corregir el frente de fase de estos chips mejorando la directividad y, por tanto, el rango de funcionamiento. Las lentes geodésicas, que pueden ser construidas utilizando sólo metales, ofrecen las propiedades atractivas de las lentes dieléctricas comunes sin sus pérdidas en el metarial.

En este trabajo de fin de máster se ha diseñado una antena del tipo lente geodésica específica con propiedades de enfoque para mejorar las capacidades de imagen de radar del transceptor TRA-120-002 que trabaja en la banda ISM de 120 GHz.

Se ha hecho un estudio de diferentes transiciones para los puntos singulares de la antena, minimizando reflexiones sin aumentar las aberraciones en la lente. En el trabajo se muestra un diseño optimizado de la apertura de la antena donde se utilizan corrugacions para mejorar el diagrama de radiación. Se ha diseñado también una pequeña antena de apertura con una metasuperfície de pines periódicos para maximizar la transmisión de energía entre el transceptor COTS y la lente. Finalmente, se ha añadido una metasuperfície basada en agujeros con simetría deslizada para evitar fugas entre las placas de la antena debido a posibles limitaciones en su fabricación.

Los resultados muestran que se puede conseguir una antena de tipo lente de 5λ de radio totalmente metálica con directividad superior a 19,5 dB y niveles de lóbulos secundários (SLL) entre -10,5 dB y -9,2 dB dentro de la banda de 119 GHz - 125,5 GHz mientras que la antena focaliza a 30 cm.

Acknowledgements

Several people have contributed to this thesis. I would firstly like to express my sincere gratitude to my supervisor Pilar Castillo for the knowledge, guidance and unending encouragement that I have enjoyed working with her.

I also would like to thank my examiner Óscar Quevedo for their invaluable suggestions during the design of the lens antenna and for give the opportunity to work on such an amazing project.

I would like to extend my thanks to KTH Royal Institute of Technology for all the facilities given during my studies.

Finally, I am thankful to all members of my family and friends for their support and encouragement. Especially to Jesús, Álvaro and Federico among other colleagues in the Master Student Room lab for being every day next to me during the thesis development. Finally thanks to Pau for helping me with the Runge–Kutta method.

List of Abbreviations

COTS commercial-off-the-shelf. iii, 1, 2, 4, 13, 26, 28, 41

CW Continuous Wave. 4

EBG Electromagnetic Band-Gap. iii, xviii, 28, 32, 34, 35, 37, 41

EM Electromagnetic. 3, 5

FMCW Frequency Modulated Continuous Wave. 1, 4, 26, 32, 39

GRIN Graded Index. xvii, 7–10

ISM Industrial, Scientific and Medical. iii, 2, 26

MMIC Monolithic Microwave Integrated Circuit. iii

mmW Millimiter Wave. iii, 1–5, 13, 26, 30, 32, 41–43

PMC Perfect Magnetic Conductor. 16

PPW Parallel Plate Waveguide. 2, 7, 13, 14, 22, 23, 27, 30, 32, 37, 41

radar Radio Detection and Ranging. 1–5, 7, 13

RAR Real Aperture Radar. 1, 4, 5

RF Radio Frequency. 1

SAR Synthetic Aperture Radar. 4, 5

SLAR Side-Looking Airborne Radar. 4, 5

SLL side-lobe levels. iii, 8, 15, 28, 32, 34, 39

UWB Ultra Wide-Band. 9

Contents

List of Figures

List of Tables

Chapter 1

Introduction

1.1 Preamble

The Millimiter Wave (mmW) band is the wide band of the Radio Frequency (RF) spectrum that ranges from 30 GHz to 300 GHz. The mmW name came from the fact that the wavelengths within this band are between 1 cm and 1 mm.

This band is characterized by a high atmospheric attenuation, increasing with the frequency till an almost null transmission at the upper part of the band. There are regions of the spectrum in this band with high attenuation due to the resonance of the H_2O (at 22.3 GHz, 183.3 GHz and 323.8 GHz) and O_2 (at 60 GHz and 118.74 GHz) molecular particles [10] with transmission windows between them.

The high available bandwidth and small wavelength makes the mmW band really interesting for short range high accuracy and resolution radar applications. The high atmospheric attenuation may allow frequency re-usability but severally limits the operating range. This project is mainly focused on an antenna solution for Frequency Modulated Continuous Wave (FMCW) radar imaging working at mmW band.

1.2 Project Statement

1.2.1 Problem Definition

The advantages of increasing the FMCW radar working frequency, or being more precise, increasing the available bandwidth are explained in section 2.1.1. Nevertheless, the use of high gain antennas are needed in order to overcome the atmospheric losses and increase the angular resolution in the case of Real Aperture Radar (RAR) measurements.

The deployment of the 5G allowing ultra-reliable low latency communications is pushing the autonomous vehicle industry, where radar sensors play a crucial role in safety. The offer of RF commercial-off-the-shelf (COTS) products for research purposes at mmW has been increasing the recent years due to the market demand. Some of these COTS mmW radar solutions have the RF front-end and the antennas monolithically integrated in the same chip to offer lower size and loss.

The antennas that can be integrated in a chip have a limited aperture restricted to the physical size of the component. In order to increase the overall directivity of the radar front-end, mainly dielectric lenses are used for modifying the phase front of the radiated wave using Fermat's principle. Moreover, lenses allow the creation of image points at a specific distance which is a very important feature for short-range

measurements. The use of dielectric materials at mmW, however, yield to an important increment in the dielectric losses. This is even more accentuated in a radar system since the electromagnetic wave has to cross two times the lens before reaching the receiver. This attenuation, together with possible reflections due to medium impedance miss-match, makes the overall gain of the system relatively poor.

1.2.2 Proposed Solution

In order to overcome the high attenuation and reflections of the dielectric lenses, the use of a fully metallic Parallel Plate Waveguide (PPW) geodesic lens is proposed. In a geodesic lens, the electric field propagates mainly in air confined between a pair of metallic parallel plates, following a specific geodesic shape, derived applying transformation optics.

The main goal of this project is to demonstrate the capabilities of these lenses for radar imaging purposes at mmW using a COTS radar front-end integrated on a chip. The transceiver used is the TRA-120-002 [1] from SILICON RADAR, which is a compact IC module characterized by a high measurement resolution in the 120 GHz ISM band where its transmitter and receiver branch has separate signal lines.

The lens antenna has to be fully metallic with a diameter of 10λ at f_0=122 GHz. Moreover, the antenna has to be able to focus the source radiation to a single focal point, creating an image at 30 cm from the lens. Side lobes less than -15 dB and a reflection coefficient smaller than -20 dB are required within all the operational band of the radar (119 GHz to 125.5 GHz). In order to decrease the overall thickness of the lens antenna, it has to be folded applying mirroring [12] and having a final water-drop profile shape [13].

1.3 Outline

This project is divided into 6 sections, where in the first one the project is presented as well as the motivation of the work and the scope of the thesis is stated.

In the following section, some background is provided regarding the main concepts involved in the project. The State-of-the-art solutions found in the literature are presented and adapted to the scope of this project.

The methodology is explained within section 3, going through all the designed segments of the geodesic lens antenna and presenting the intermediate results of each one of the stages.

The final results are presented and discussed in section 4.

To conclude the thesis some overall conclusions and future work are included in section 5 and followed in section 6 by a summary of the project impact on ethics and the environment.

Chapter 2

Theory

2.1 Millimeter Wave Radar Imaging

Imaging, defined as the process of making a visual representation of something by scanning it with a detector or electromagnetic beam, includes a large variety of methodologies and technologies. Mainly it senses the signals coming from a target, being them mechanical waves like sound, electromagnetic waves or other types of sources.

In the case of Electromagnetic (EM) imaging, the most common type of imaging, the image is created after the processing of the scattered, reflected, diffracted or emitted EM signal by the target area or body. We can distinguish between passive systems like the spectrometer or radiometer and active ones like radar or lidar.

Both systems have a receiver that gathers the signal from a specific spot or area, which is related to the system resolution. Then, with different processing of those signals, several information and images can be generated depending on the application and the working frequency band. Not only the geometry and shape can be obtained but also the electrical properties of the target materials, the presence of some specific element, etc. While the passive systems use an externals source of energy to illuminate the target like the Sun in optical imaging, the target body itself for thermal imaging or even the GNSS signals, the active systems illuminate the target itself transmitting a high power signal to the area of interest.

Radar, which is an acronym for RAdio Detection And Ranging, is an active detection system that uses radio waves to determine the range, angle, or velocity of objects by echo-location. It was developed during World War II for military purposes. Modern uses of radar, however, are highly diverse like astronomy, defence, surveillance, imaging, meteorological, guidance, etc.

Millimeter wave (mmW) imaging can complement optical systems overcoming some of their limitations. Even though they do not achieve the same resolution, which is tighten to the wavelength, they can perform night imaging, see through materials and even sense over adverse weather conditions like rain or fog. All these properties makes the mmW band interesting in the field such navigation, security, material characterization, 3D imaging or high accuracy and resolution measurements.

2.1.1 FMCW Radar

Radars can be classified into pulsed or continuous wave based on the type of signal with which radars can be operated. In this project, we are mainly interested in

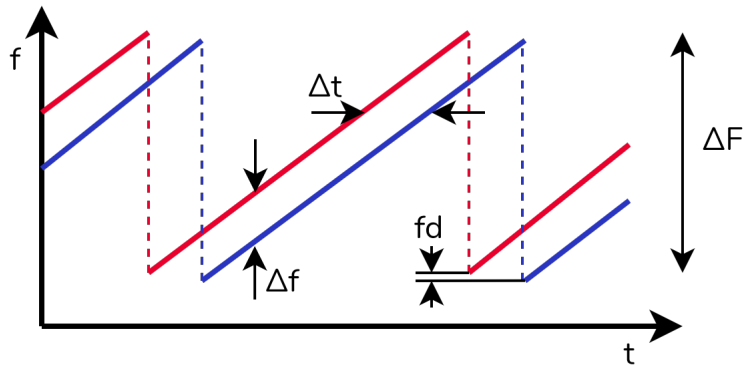

FIGURE 2.1: Transmitted (red) and received (blue) signals as a function of the time.

FMCW radars, which is a specific case of CW radar, since is the type of the COTS transceiver used.

FMCW radars continuously transmit a frequency modulate signal while they receive the target echo in a separated antenna. The modulation of the transmitted signal allows to create a time reference so that the target range can also be determined. As shown in Figure 2.1, the received signal is delayed (Δt) with respect to the transmitted one in function of the target position and shifted (fd) in function of the target radial speed due to the Doppler effect. The echo received Δt seconds later is mixed with a portion of the transmitted signal to produce a beat signal at a frequency Δf which is used together with the modulation scheme in order to compute the target range and velocity.

The range resolution of a FMCW radar is related to their frequency resolution, which depends on the bandwidth of the modulated signal ΔF. Being c the speed of light, we have:

$$\Delta r = \frac{c}{2 \cdot \Delta F} \tag{2.1}$$

From Equation 2.1 one can quickly see one of the advantages that offer the mmW band with respect to other ones at a lower frequency with a more restricted available bandwidth.

2.1.2 Radar Imaging techniques

From radar measurements information of scattered power, ranging and radial velocity can be acquired. If there is a relative linear traversal or angular movement between the radar and the target, the measurements of each pixel can be plotted in a 2D or 3D image. There are several ways and techniques to perform images from radar. The most common ones are Real Aperture Radar (RAR) or Side-Looking Airborne Radar (SLAR) and Synthetic Aperture Radar (SAR).

RARs have a moving platform that produces a beam thin in the direction of the movement and wide in the transverse one with a looking angle greater than 0°. The reflections from the furthest points located within the illuminated area arrive with a time delay proportional to the slant range. Hence, the range direction of the image can be obtained through ranging measurements. During the next stripe processing,

the radar will have moved forward a specific distance, covering a new region within the antenna beam-width. All these measured regions can be concatenated to build up the azimuth direction.

The resolution in the azimuth axis is the ability of the radar to discriminate to physical separated scatters in the direction parallel to the moving sensor. In the case of RAR or SLAR it is represented by the half-power beam-width of the antenna used and can be approximated by:

$$\Delta a \geq 2R \sin \frac{\theta_{-3dB}}{2} \tag{2.2}$$

Where Δa is the azimuth resolution in meters, R is the slant range and θ_{-3dB} the antenna half-power beam-width. From Eq. 2.2 it can be seen that high resolutions can be achieved at distances near the source. The increase of the antenna size and going up in frequency will lead to an increase of the antenna gain, or equivalently, a decrease in the beamwidth allowing to improve the resolution in the azimuth axis.

The other imaging technique using SAR overcomes the problem of needing an electrically big antenna by signal processing. In SAR low or medium gain antennas are used and extremely high resolutions in azimuth can be achieved by processing the Doppler shift information. This technique, detailed in [5], is mainly used for remote sensing applications [3] where the slant range is huge and the physical size of the antennas is limited.

Due to the atmospheric attenuation of the signal at mmW, medium-range imaging is not feasible without high gain antennas. Furthermore, at those frequencies, high gain can be achieved through a physically small antenna. These two factors combined make very interesting the high resolution, short-range RAR imaging where lens-type antennas play a key role, especially for chip-integrated feeds.

2.2 Lens Antennas

A lens antenna is a type of aperture antenna that makes use of lenses to modify the phase front of an incoming EM wave. In order to produce a narrow beam, they need to have an electrically large aperture, typically more than 5λ of diameter. This is why this type of antennas are mainly used at high frequencies and have recently become popular for applications at Ka, mmW and THz bands.

Lens antennas can be designed making use of ray theory and geometric optics then physical optics and theory can be used to simulate the antenna behaviour at microwave frequencies with more accurate results.

A lens is a wide-band transmissive device mainly used in optics with the ability to focus or disperse an incoming ray beam by means of refraction. They are designed making use of the law of reflection (Eq. 2.3) and the Snell law (Eq. 2.4) in order to bend the incoming ray. Where from Figure 2.2 the θ_i, θ_t and θ_r are the incident, transmitted and reflected angles when the ray transits between a medium with refractive index n_1 to a medium with refractive index n_2.

$$\theta_i = \theta_r \tag{2.3}$$

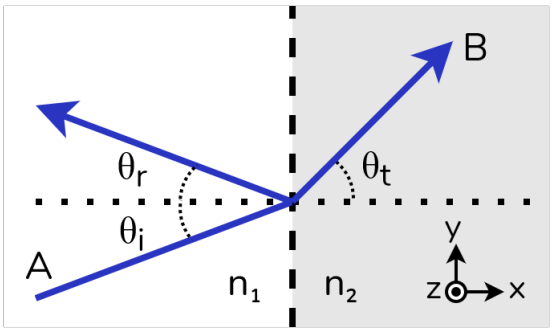

FIGURE 2.2: Refraction and reflection of an incoming ray

$$n_1 \sin(\theta_i) = n_2 sin(\theta_t) \tag{2.4}$$

Fresnel equations are used then to find the magnitude and phase of the transmitted and reflected electric fields. The incident signal can be split into a combination of two orthogonal polarizations with their respective two different Fresnel coefficients.

For the electric field $E_\perp$ normal to the plane of incidence (XY in Figure 2.2) we have the following transmition $t_\perp$ and reflection $r_\perp$ coefficients:

$$t_\perp = \frac{2n_2 \cos\theta_i}{n_1 \cos\theta_i + n_2 \cos\theta_t} \tag{2.5}$$

$$r_\perp = \frac{n_1 \cos\theta_i - n_2 \cos\theta_t}{n_1 \cos\theta_i + n_2 \cos\theta_t} \tag{2.6}$$

And for the electric field component parallel to the incidence plane $E_\parallel$ we have:

$$t_\parallel = \frac{2n_2 \cos\theta_i}{n_2 \cos\theta_i + n_1 \cos\theta_t} \tag{2.7}$$

$$r_\parallel = \frac{n_2 \cos\theta_i - n_1 \cos\theta_t}{n_2 \cos\theta_i + n_1 \cos\theta_t} \tag{2.8}$$

Lenses can be designed to converge, diverge or collimate incident rays. A converging lens focuses a beam travelling along the lens axis to a spot (known as the focal point) at a specific focal distance from the lens. If an object is placed in that focal point, an image of this object is projected to the source point or to the infinity in case that the incident rays are collimated. If the object is, however, placed at a distance less than the focal distance, the lens then has magnifying properties. These lenses are widely used for optical imaging in cameras, telescopes and the human eye.

Converging lenses can be used as well as antennas, where the lens radiates the energy from a point source to a given direction when transmitting or focus all the energy received from a specific direction to a single reception point.

From Fresnel equations and the reflection and Snell law, it can be seen that the phase front of incoming radiation can be modified (or thinking in the ray theory the incident rays can be tilted) by shaping the lens geometry or gradually varying the

electrical properties of the lens material. We can find, then, several types of lenses regarding the way they are constructed and briefly detailed in the next section.

2.2.1 Types

Homogeneous lens

Homogeneous lenses use their geometry for changing the incident angle θ_i (and the transmitted θ_t as well due to Eq. 2.4) keeping the lens dielectric material properties n_2 constant. They have the advantage that can be easily manufactured but suffer from high reflections due to impedance miss-match in the medium discontinuities.

Graded index lenses

The Graded Index (GRIN) lenses, however, are constructed with a varying refractive index $n_2(r, \phi)$ dielectric material that smoothly curves the incident ray while it propagates through the lens. For some of the lenses, the refractive index $n_2(r, \phi)$ is found solving the inverse Luneburg problem [18] specifying a source and an image point coordinates. The Luneburg problem lenses can be solved so they have the same refractive index in the lens edge than the medium ($n = \sqrt{\epsilon_r \mu_r} \approx 1$ for air) so no reflections are generated at the lens edge, overcoming one of the biggest problems of the homogeneous lenses by increasing their manufacturing complexity.

They are rotationally symmetric so $n_2(r, \phi) = n_2(r)$ so they also have the advantage of being capable of beam steering by changing the position of the source. Spherical media has firstly been described by James Clerk Maxwell in 1854 introducing Maxwell's fish-eye lens [15], where all the rays from a source point located in the lens edge converge to a single focal point in the opposite side of the lens creating a perfect image. Luneburg [14] derived the refractive index of a lens which focuses a collimated beam into a single point on its opposite surface. Luneburg lenses have been popular for high frequency communications and radar applications due to their high directivity with a big scanning range. Other interesting rotationally symmetric GRIN lenses are the Eaton lens and the 90º rotating lens which rotate a beam of parallel rays 180º (working as a retro-reflector) and 90º respectively.

Artificial dielectric lenses

The artificial dielectric lenses are lenses built using meta-surfaces that simulates the behaviour of dielectric lens within a specific narrow frequency band. They can be used to manufacture GRIN lenses with homogeneous materials. The use of meta-surfaces also allows making lenses that propagate within the air with an enclosed 3D metallic structure, avoiding the dielectric losses at high frequencies.

Geodesic lenses

The geodesic lenses are lenses made of structures that control the direction of the microwaves. They have a 3D geodesic shape where the radiation is confined within a Parallel Plate Waveguide (PPW) and commonly it propagates through air, avoiding reflections due to medium impedance mismatch and having low losses at high frequencies. Since this type of lenses modifies the phase front of the incoming signal through a true-time delay, they are wide-band antennas. Geodesic lenses are furtherly discussed in section 2.2.4.

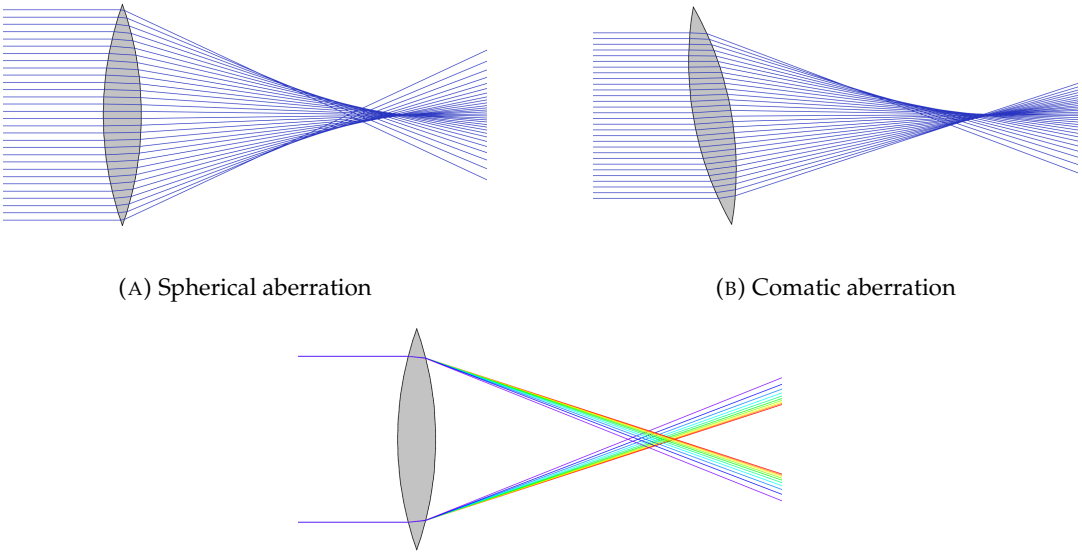

(A) Spherical aberration

(B) Comatic aberration

(C) Chromatic aberration

FIGURE 2.3: Examples of optical aberrations in lenses.

2.2.2 Aberrations

Imperfections in the lens design can cause rays to not converge in a single focal point but spread in a region of space. This property, known in optics as aberration, directly affects the performance of an imaging system, causing the image of the object blur or distort from the ideal one. If the lens is used as an antenna, where the source phase center must be located in the lens focal point, aberrations in the lens will cause a distortion in the radiated field with a decrease in the antenna directivity and an increase of the antenna side-lobe levels (SLL).

Regarding the nature of the aberration, we can find two different types: Monochromatic and chromatic ones. The former aberrations do not consider the effect the frequency of light has on its propagation through a system. They are typically related to the paraxial approximation and can be caused by several factors. The presence of a spherical curve causes spherical aberrations, shown in Figure 2.3a). A non-null angle between incident rays that pass through the lens with respect to the focal axis cause what is called coma, shown in Figure 2.3b. Also, the lens can behave different regarding the polarization, having different focal points which cause the astigmatism.

The chromatic aberrations, however, are caused by a dispersive behaviour of the lens, where the focal length is frequency dependant as illustrated in Figure 2.3c. This property, however, can be used to compensate for a possible dispersive feeder decreasing the overall chromatic aberrations.

2.2.3 Transformation Optics

The properties of the GRIN lenses are of high interest for many applications. However, their physical implementation is not always possible due to the inability to produce a non-homogeneous distribution of the refractive index. Discretizing the lens and using homogeneous materials has been used as well as the use of metasurfaces.

In order to keep the Ultra Wide-Band (UWB) property of the lenses while using a single homogeneous material, transformation optics can be used. It stands for the capability of bending light, or electromagnetic waves and energy, in any preferred or desired fashion, for a desired application. The lens permittivity ϵ_r and permeability μ_r represents, for the light, a curved spatial geometry in the real space. This curved geometry is obtained by applying transformations optics to a reference flat virtual space. The Maxwell equations maintain the same form under a coordinate transformation so they maintain invariant, allowing a correspondence between a coordinate transformation and electrical properties of a material known as conformal mapping.

This property was applied in lenses design by Rinehart, who in [17] replaced the central sections of spherical lenses by equivalent curved two-dimensional surfaces with rotational symmetry and constant refractive index.

2.2.4 Geodesic Lenses

As mentioned before, geodesic lenses are lenses that confine the electric field and makes it propagate through a specific curved geometry. The shape of a geodesic curve whose axis of symmetry is equivalent to the z axis shown in Figure 2.4, can be described with a radial coordinate ρ, an angular coordinate θ and the length $s(\rho)$ of a specific point from the axis of symmetry measured in the geodesic surface along their meridian.

The function $s(\rho)$ can be found solving the inverse Luneburg problem for a specific source and image points and replaces the desired $n(r)$ for a homogeneous solution applying transformation optics.

The coordinate transformation between a GRIN and a geodesic lens comes from the fact that the optical path elements of both lenses must be equivalent. Fermat's principle states that light travels between two points along the path that requires the least time. The optical path can be then defined as:

$$\sigma = \int_A^B n(s)\, ds \tag{2.9}$$

And its element:

$$d\sigma = n\, ds \tag{2.10}$$

Where ds is the geometrical length among the path A-B of the ray. It can be expressed in Cartesian coordinates as:

$$ds = \sqrt{dx^2 + dy^2 + dz^2} \tag{2.11}$$

For the case of a planar in-homogeneous lens, shown in Figure 2.5, the square root of the optical path element can be defined as:

$$d\sigma^2 = n^2(dr^2 + r^2 d\phi^2) \tag{2.12}$$

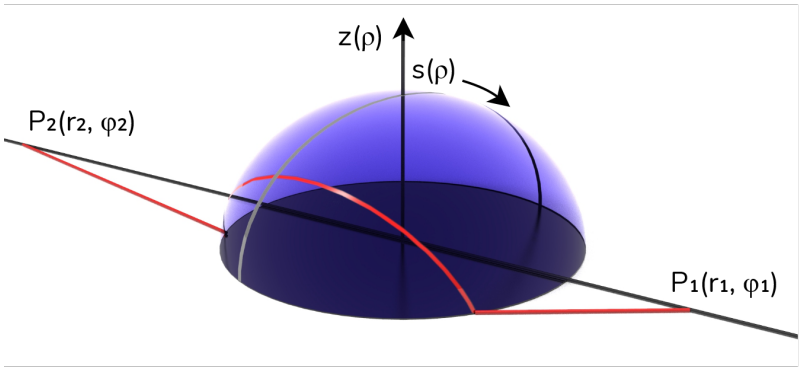

FIGURE 2.4: Ray path within a geodesic lens

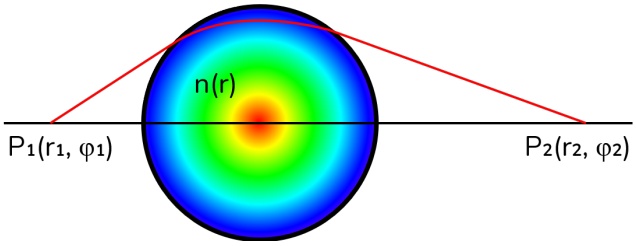

FIGURE 2.5: Ray path within a GRIN lens

The square root of the optical path element of a ray following a geodesic surface is shown in Figure 2.4 and can be defined as:

$$d\sigma^2 = ds^2 + \rho^2 d\theta^2 \tag{2.13}$$

Equating both optical paths Eq. 2.12 and Eq. 2.13 and setting $\phi = \theta$ we find the following relations that completely determine the conformal mapping between a GRIN lens and its equivalent geodesic shape:

$$\begin{cases} \rho = n\, r \\ ds = n\, dr \end{cases} \tag{2.14}$$

We can assume now a system of polar coordinates (r, ϕ) and a lens of radius equal to 1 with the center at the origin. Solving the inverse Luneburg problem for a specific source $P_1(r_1, \phi_1)$ and image $P_2(r_2, \phi_2)$ points and applying Eq. 2.14 one can derive the shape of the geodesic curve s in function of the distance to the axis of symmetry ρ. The derivation, which can be found in [18], is not included here since it is out of the scope of this work. The final expression of $s(\rho)$ is provided in the following equation, where $-M\pi$ is the total change of polar angle swept by the light ray during

its propagation from the source to the image ($M = 1$ for a Luneburg lens):

$$\begin{aligned} s(\rho) = &-\frac{1}{\pi}\Bigg[\rho \arcsin\left(\sqrt{\frac{1-\rho^2}{r_1^2-\rho^2}}\right) + \rho \arcsin\left(\sqrt{\frac{1-\rho^2}{r_2^2-\rho^2}}\right) \\ &+ r_1 \arcsin\left(\rho\sqrt{\frac{r_1^2-1}{r_1^2-\rho^2}}\right) + r_2 \arcsin\left(\rho\sqrt{\frac{r_2^2-1}{r_2^2-\rho^2}}\right) \\ &- \sqrt{r_1^2-1}\arcsin(\rho) - \sqrt{r_2^2-1}\arcsin(\rho) \\ &- \arcsin\left(\frac{1}{r_1}\right)\arcsin(\rho) - \arcsin\left(\frac{1}{r_2}\right)\arcsin(\rho)\Bigg] \\ &+ (M-1)\arcsin(\rho) + \rho \end{aligned} \tag{2.15}$$

In order to build the lens, however, it is more useful to express the geodesic shape in Cartesian coordinates $z(\rho)$ rather than $s(\rho)$ as shown in Figure 2.4. This functions are related by:

$$dz = \pm\sqrt{ds^2 - d\rho^2} \tag{2.16}$$

Here it is important to notice that for a specific ds two solutions (positive and negative) of dz are valid. This property was used by Kunz [12] in order to apply mirroring to the geodesic shape and decrease the overall lens height. Then, computing ds from Eq. 2.15 and substituting to Eq. 2.16 we obtain:

$$\begin{aligned} \mathrm{dz} = \mp\Bigg[&\frac{1}{\pi^2}\Bigg(\frac{\pi(M-1) + \arcsin\left(\frac{1}{r_1}\right) + \arcsin\left(\frac{1}{r_2}\right) + \sqrt{{r_1}^2-1} + \sqrt{{r_2}^2-1}}{\sqrt{1-\rho^2}} \\ &- \arcsin\left(\sqrt{-\frac{\rho^2-1}{{r_1}^2-\rho^2}}\right) - \arcsin\left(\sqrt{-\frac{\rho^2-1}{{r_2}^2-\rho^2}}\right) \\ &- \frac{r_1}{\sqrt{1-\frac{\rho^2({r_1}^2-1)}{{r_1}^2-\rho^2}}}\left(\sqrt{\frac{{r_1}^2-1}{{r_1}^2-\rho^2}} + \frac{\rho^2\left({r_1}^2-1\right)}{\sqrt{\frac{{r_1}^2-1}{{r_1}^2-\rho^2}}\left({r_1}^2-\rho^2\right)^2}\right) \\ &- \frac{r_2}{\sqrt{1-\frac{\rho^2({r_2}^2-1)}{{r_2}^2-\rho^2}}}\left(\sqrt{\frac{{r_2}^2-1}{{r_2}^2-\rho^2}} + \frac{\rho^2\left({r_2}^2-1\right)}{\sqrt{\frac{{r_2}^2-1}{{r_2}^2-\rho^2}}\left({r_2}^2-\rho^2\right)^2}\right) \\ &+ \frac{\rho^2\left({r_1}^2-1\right)}{\sqrt{-\frac{\rho^2-1}{{r_1}^2-\rho^2}}\left({r_1}^2-\rho^2\right)^2\sqrt{\frac{\rho^2-1}{{r_1}^2-\rho^2}+1}} \\ &+ \frac{\rho^2\left({r_2}^2-1\right)}{\sqrt{-\frac{\rho^2-1}{{r_2}^2-\rho^2}}\left({r_2}^2-\rho^2\right)^2\sqrt{\frac{\rho^2-1}{{r_2}^2-\rho^2}+1}} + \pi\Bigg)^2 - 1\Bigg]^{\frac{1}{2}} \end{aligned} \tag{2.17}$$

The equivalent geodesic lenses for different solutions of the Luneburg problem are shown in Figure 2.6 together with a simulation of every lens in CST.

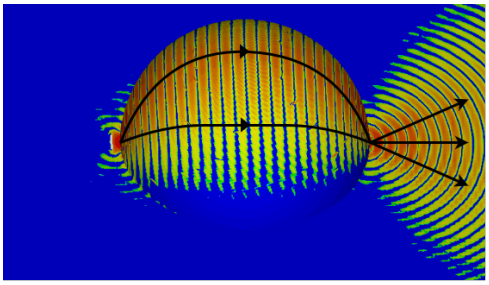

(A) Maxwell fish-eye lens [15]
($r_1 = r_2 = 1$, $M = 1$)

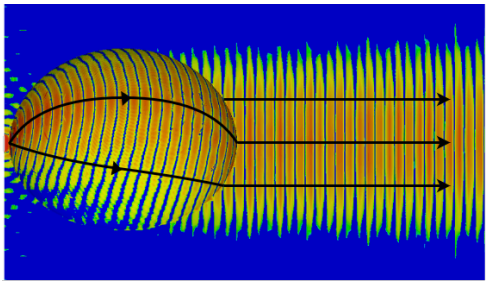

(B) Luneburg lens [14]
($r_1 = 1$, $r_2 = \infty$, $M = 1$)

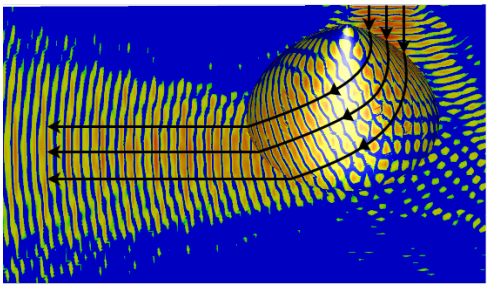

(C) 90º rotating lens
($r_1 = r_2 = \infty$, $M = 3/2$)

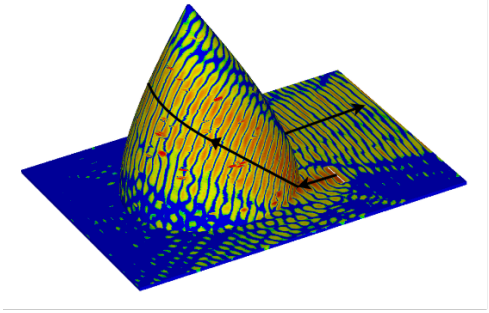

(D) Eaton lens [6]
($r_1 = r_2 = \infty$, $M = 2$)

FIGURE 2.6: Simulated electric field through equivalent geodesic lenses for different solutions of the Luneburg problem with the ray tracing overlayed.

Chapter 3

Methodology and Implementation

This chapter goes through all the designing processes and simulations of a fully-metallic focusing geodesic lens antenna used for radar imaging at mmW band using the COTS *TRA-120-002* transceiver from SILICON RADAR [1] as a source and receiver.

This solution is expected to overcome the high losses that suffers a mmW signal when going through a conventional dielectric lens. These losses, that are accentuated in radar imaging techniques by the fact that the signal needs to cross the antenna in two ways, together with reflections due to impedance miss-match, make the fully metallic geodesic lens antenna a good candidate for these systems.

For the antenna designing, some constraints were set as well as several requirements to be fulfilled. Table 3.1 summarizes them.

Parameter	**Value**
Frequency band (central)	119 GHz - 125.5 GHz (122 GHz)
Antenna radius	12.3 mm (5 λ)
Focal distance	30 cm - 3 m (122 λ - 1220 λ)
Antenna foldings [12]	1
Antenna return losses	< -20 dB
Antenna SLL	<-15 dB

TABLE 3.1: Design constrains and antenna requirements

The overall antenna is composed of different parts or sections that have been independently designed and optimized before the overall antenna integration and simulation. Those parts, which include the lens shape, the discontinuities in that geodesic shape, the radiating flare and the lens antenna feeder are detailed described in this chapter as well as the overall integration.

3.1 Geodesic Shape

A geodesic lens, as mentioned in Section 2.2.4, is a lens that makes use of an extra spatial coordinate in order to build an equivalent lens for a specific solution of the Luneburg problem using transformation optics. The rays are confined between two metallic plates, structure known as Parallel Plate Waveguide (PPW), and forced to follow a specific geodesic curve defined in Eq. 2.15.

In order to find the desired geodesic shape, Eq. 2.16 has been numerically integrated using the classic 4^{th} order Runge-Kutta (RK4) method [2] forcing the lens height z

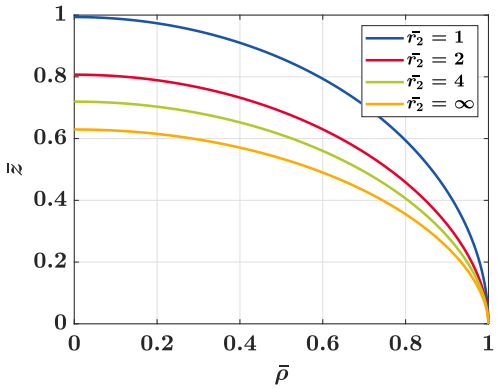

FIGURE 3.1: Normalized geodesic lenses profile for different normalized focal distances.

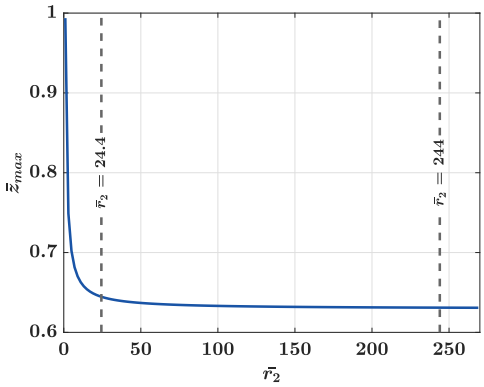

FIGURE 3.2: Normalized lens height for different normalized focal distances.

to be zero at the antenna edge $\rho = 1$ and integrating backwards till the lens axis of symmetry where the height is maximum:

$$z_0 = z(1) = 0 \tag{3.1}$$

The computed profile of a geodesic lens with a source point located in the lens edge $\bar{r_1} = 1$ for different focal distances is shown in Figure 3.1. Where $\bar{\rho}$, $\bar{z}$ and $\bar{r_2}$ are the radial distance, height and focal distance of the lens normalized with respect to their radius. It can be shown that the overall height of the lens is decreased as the focal distance is increased, going from $\bar{z} = 1$ lens radius for the well known Maxwell fish-eye lens till $\bar{z} \approx 0.63$ lens radius for the Luneburg lens.

Figure 3.2 shows the non-linear relation between the lens height and the focal distance being the height change almost negligible at long focal distances. In that image, focal distances of 24 and 244 times the lens radius are marked. Those distances are the equivalent ones for a 5λ radius lens at 122 GHz that focalizes at 30 cm and 3 m. Here we can see that a geodesic lens that fulfils the specifications of Table 3.1 differs in height by 0.015 mm and 0.001 mm from the Luneburg lens. This means that the designed antenna for imaging purposes will perform very similar for targets located at 30 cm, 3 m or further away in terms of focus. Furthermore, some of the merit parameters for Luneburg lens antennas like the directivity can be used to check the designed antenna performance (but not for optimization). For having a precise focal point at those physical distances a much bigger lens would be needed so $\bar{r_2} < 10$.

Parallel Plate Waveguide (PPW)

As mentioned before, a geodesic lens must constrain the electric field between two metallic plates in order to force the rays to follow a specific path. A symmetrical offset has been applied to the curve obtained through the RK4 in order to generate the plates that form the PPW. Both plates must differ from the theoretical curve an identical distance in order to avoid aberrations in the lens.

Within a PPW, the TEM mode is propagated. We must guarantee, however, that no higher-order modes are allowed within the structure since they will propagate with

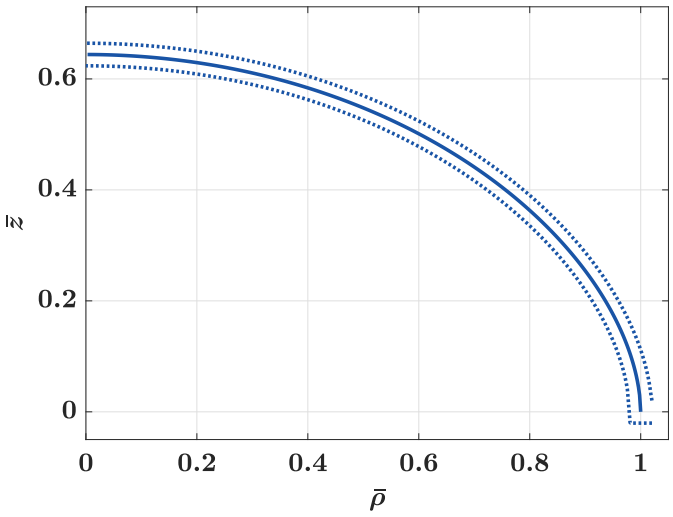

FIGURE 3.3: Geodesic lens profile for a focal distance of $\bar{r}_2$ = 30 cm. Dashed lines represent the metallic plates shape with an offset of $h/2$ = 0.25 mm from the theoretical curve (continuous line).

different speeds than the TEM mode. The next modes that can be generated are the TE and TM ones with a cut-off frequency:

$$f_c = \frac{m}{2h\sqrt{\mu\epsilon}} \tag{3.2}$$

Where m is the mode number (TE_m or TM_m) and h the distance between the metallic plates. For guaranteeing that the lens work at the monoband region in all our band and assuming that the wave propagates mainly in air ($v_p = c_0$), the distance between plates must fullfil:

$$h < \frac{c_0}{125.5 \cdot 10^9 \cdot 2} \approx 1.2mm \tag{3.3}$$

A safe distance between plates of h = 0.5 mm was selected in this work.

The plates profile shown with a dashed line in Figure 3.3 were exported from MATLAB to CST for doing the full wave simulations.

Chamfers

From Eq. 2.17 it can be seen that $|dz| \to \infty$ at the antenna edge $\rho = 1$. This yields to an abrupt change of the light pass direction. At those transitions, the electromagnetic wave suffers from high reflections degrading the antenna performance in a noticeable way by means of an increase of the reflection coefficient $|S_{11}|$ and the SLL.

In order to decrease the effect of this abrupt change in dz, three different transitions have been studied: the toroidal bend, the symmetric and the asymmetric chamfer. The common idea behind them is to make the lens height change smooth so less

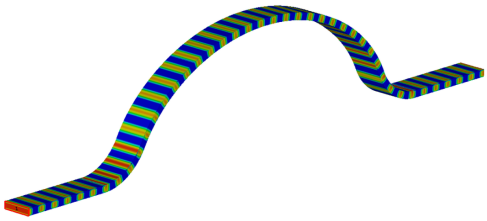

(A)

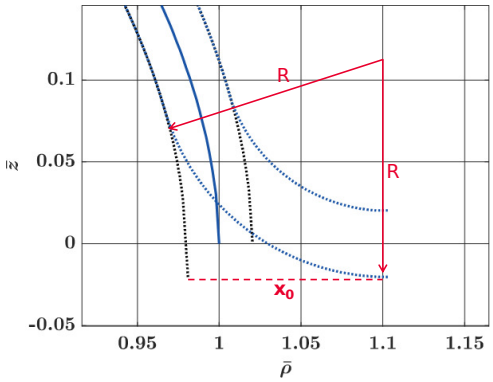

(B)

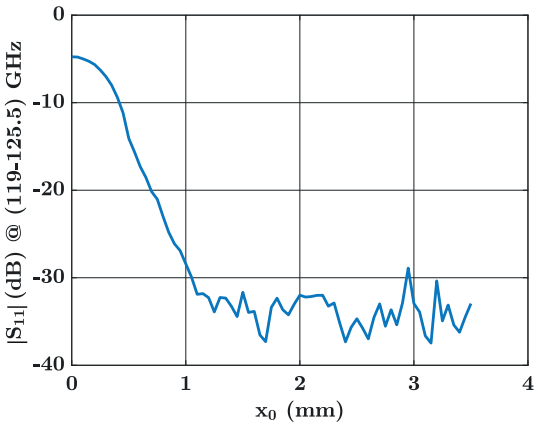

(C)

FIGURE 3.4: (A) Simulated electric field through a focusing lens 2D cut ended with a toroidal bend. (B) Profile of the toroidal bend with radius R. (C) Maximum value of the $|S_{11}|$ within the working band in function of the lens extension x_0.

energy is reflected. However, since the geodesic shape has been specifically computed for ensuring that the rays converge at a specific image point, any change or difference in that shape will introduce aberrations.

The toroidal bend consists of shaping the lens edge substituting it with a specific curve. This function is selected so it has a continuous first derivative decreasing till a null derivative at the edge. The rounded edge is used to reduce the scattering due to the steep rim between the waveguide and the lens. The effects of edge-rounding in geodesic lenses has been studied in [19] where it has been found that edge-rounding has very little effect on lens aberrations. To be more precise, for slight roundings the focal length for paraxial rays is slightly increased while for greater rounding, a decrease in focal length results from the increased optical path. In **[Kassai1979ABERRATION-CORRECTEDLENSES.]** a method for correcting the aberrations introduced by a rounded edge is proposed, where the geodesic shape is modulated so it compensates for the optical path change. This correction or similar ones, however, are out of the scope of the thesis and not implemented.

The studied solution in this work is shown in Figure 3.4a. A circular curve has been used with a turning radius R so it guarantees the continuity of the first derivative. This radius increases with x_0, which is the extension of the lens inner edge and our design parameter. A full-wave simulation has been performed in CST using a 2D geodesic lens slice with toroidal bends in the edges as shown in Figure 3.4b and using the dimensions from Table 3.1. In the simulation, a TEM mode was excited from one of the edges and PMC boundaries were used on the sides to guarantee the propagation of the fundamental mode. This simulation is close to reality only for

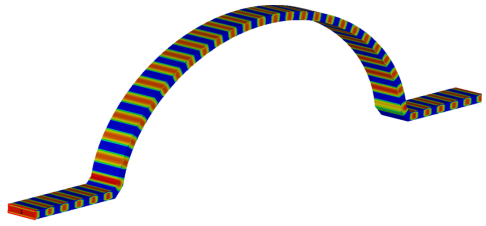

(A)

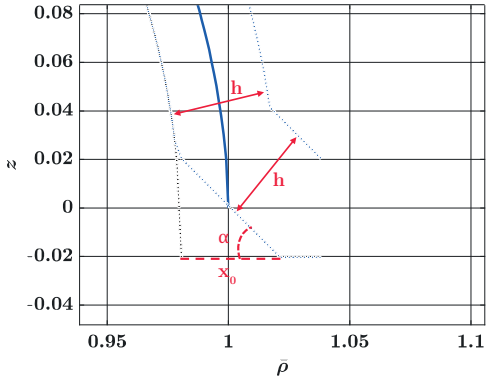

(B)

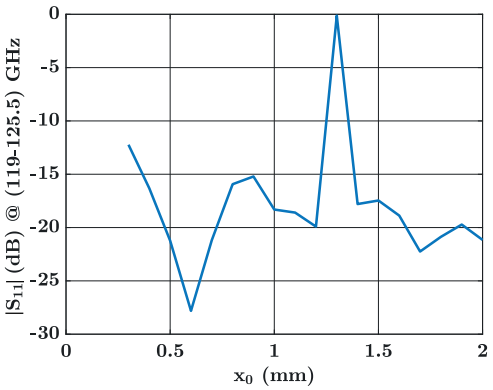

(C)

FIGURE 3.5: (A) Simulated electric field through a focusing lens 2D cut ended with a symmetric chamfer. (B) Profile of the symmetric chamfer. (C) Maximum value of the $|S_{11}|$ within the working band in function of the lens extension x_0.

the normal ray incidence but not for the oblique ones.

The maximum value of the reflection coefficient within the working frequency band in function of x_0 is shown in Figure 3.4c. It can be seen in a clear way the improvement of using rounded-edges, decreasing the $|S_{11}|$ from > -5 dB for no-bend case till < -33 dB for $x_0 > 1.2$ mm ($\approx$ 10 % of the lens radius).

The approach of the chamfered transitions is slightly different. With a chamfer, a sharp transition between the waveguide and the lens can be achieved without having a high amount of reflections. The design is done applying ray theory and the chamfer is designed using Snell's law in a way that the rays coming from the waveguide are reflected directly to the lens. With this sharp transition, we are able to improve the possible aberrations since the geodesic shape is almost completely preserved. On the other hand, the appearance of sharp edges will make the signal scatter in the transition.

The symmetrical chamfer transition is shown in Figure 3.5a and detailed in Figure 3.5b, where both plates are chamfered preserving the distance between plates h = 0.5 mm. Here the same simulation done for the toroidal bend case was performed. The maximum $|S_{11}|$ value within the working frequency band in function of the lens inner edge extension x_0 is shown in Figure 3.5c. For the simulation was fixed to 45º. In this case, the $|S_{11}|$ is below -15 dB for $x_0 > 0.4$ mm but some resonances appear at certain distances.

Finally, the same study has been done for the asymmetric chamfer case, shown in Figure 3.6a and detailed in Figure 3.6b. In this case, the chamfer is only applied to the inner plate, leaving the sharp transition in the other plate. The simulation results plotted in Figure 3.6c show that there is an optimal chamfer extension of

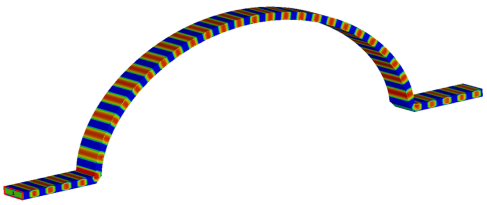

(A)

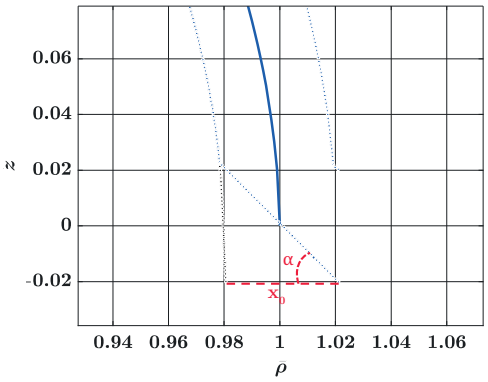

(B)

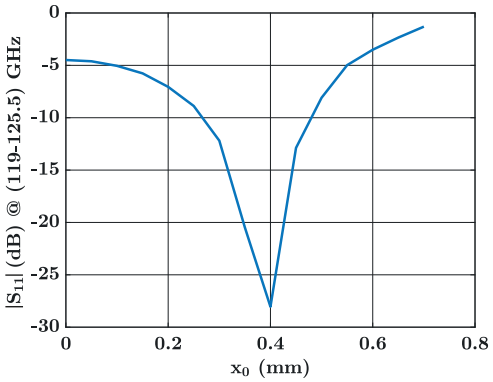

(C)

FIGURE 3.6: (A) Simulated electric field through a focusing lens 2D cut ended with a asymmetric chamfer. (B) Profile of the asymmetric chamfer. (C) Maximum value of the $|S_{11}|$ within the working band in function of the lens extension x_0.

x_0 = 0.4 mm where $|S_{11}|$ is < -27 dB. The fact that low reflections can be achieved without changing the geodesic shape and current manufacturing tolerances allow the realization of such chamfer, this solution has been adopted for the focusing lens done in this work.

When implementing the solution for the 3D shape, however, the results obtained are slightly different than the 2D simulations, where an increase in the $|S_{11}|$ is measured. As mentioned before this is due to the existence of rays with oblique incidence to the chamfers as shown in purple in Figure 3.7a. A chamfer optimized for normal incidence may perform in a sub-optimal way for other incidence angles. However, 2D simulations have been performed as a first step in order to grossly characterize the behaviour of the structure before running computationally costly 3D simulations for having precise results. Since we want to design a rotationally symmetric antenna, a full-wave simulation has been done of the 3D structure in order to find the optimal chamfer extension x_0 that minimizes the overall reflections. The results plotted in Figure 3.7b and 3.7c show that $|S_{11}| < 17$ dB can be achieved within all the frequency band using a chamfer with an extension of x_0 = 0.28 mm, value used in the design of the focusing geodesic lens.

The periodic behaviour of the $|S_{11}|$ with local minimums separated 5.14 GHz can be understood as the effect of having reflections in both the entering and exiting transitions to the lens:

$$d = \frac{c_0}{5.14\,\text{GHz}} \approx 58\,\text{mm} \tag{3.4}$$

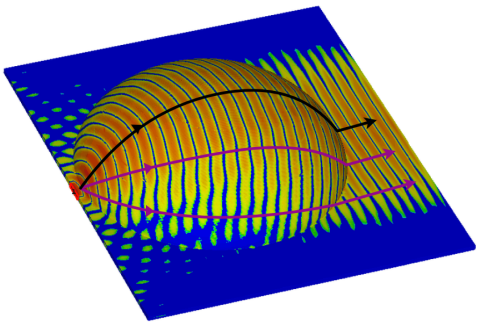

(A)

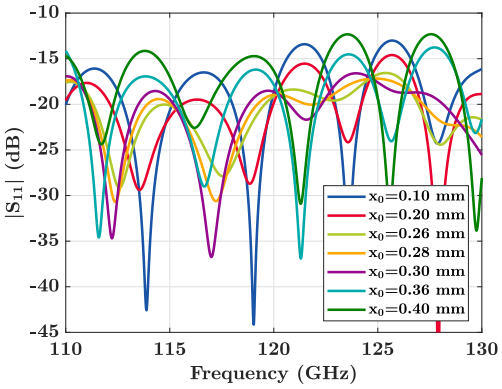

(B)

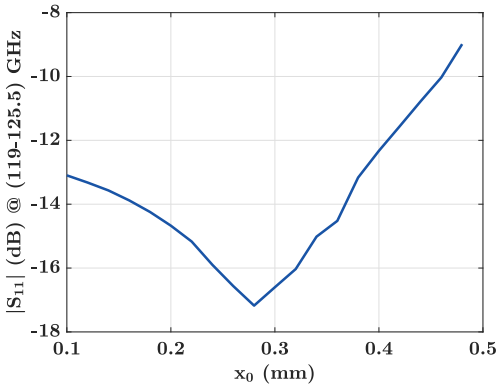

(C)

FIGURE 3.7: (A) Simulated electric field through the focusing lens with asymmetrical chamfered edges. (B) Reflection coefficient for different lens extension x_0 . (C) Maximum value of the $|S_{11}|$ within the working frequency band in function of x_0 .

Where d is equivalent to the round trip distance travelled by a ray that is reflected at the lens edge and measured at the source port.

Water-drop shape

Lens antennas are characterized for being bulky antennas. Their height, being for the case of the Luneburg lens $\bar{z} \approx 0.63$ lens radius, is often a limiting factor for some specific applications. Space sector and lens arraying are two examples where this parameter plays a critical role and the default geodesic lens is not an eligible solution [4].

To reduce the height of the geodesic lens, it can be folded as suggested by Kunz [12] applying symmetry by mirroring the curve with respect to the plane perpendicular to the lens revolution axis (z in Figure 2.4). As seen in Eq. 2.16, changing the sign of dz has no impact on the optical path length which remains equivalent after mirroring the curve. Therefore, the resultant folded lens will still be a valid solution for the specific Luneburg problem preserving the focusing properties.

A smart variation of Kunz's folding principle is explained in [8], where the height offset is symmetrical with respect to the lens edge, giving a shape looking like water drop ripples and named water-drop lens in [7]. Taking into account the symmetrical aperture horn needed for impedance matching, this solution generally yields to a lens with a thinner profile. Figure 3.8 illustrates this folding principle where the

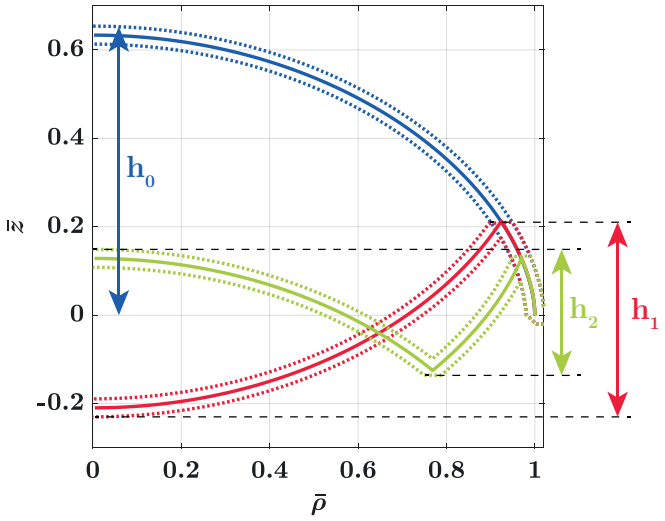

FIGURE 3.8: Geodesic profile of a focusing lens with no foldings (blue), one folding (red) and two foldings (green).

resultant lens has an overall height of:

$$h_k = \frac{2\,h_0}{2k+1} \tag{3.5}$$

Where k is the number of reflective symmetries applied.

Each one of the mirrorings, however, introduces a sharp change in the propagation path. These abrupt transitions generate reflections inside the lens that should be mitigated in order to preserve the desired phase front at the lens output. Similar as done in the lens edge, bends and chamfers can be applied to make the transitions smoother. The replacement of the singularities in the profile of the lens introduces aberrations, that limits the height reduction that can be achieved using this method. Typically no more than 3 foldings are done.

In our specific case, only one reflective symmetry has been done due to the antenna size constraints. An asymmetrical chamfer (described in section 3.1) has been used to replace the sharp transition. With this solution, the modification of the geodesic profile is minimum so we mitigate the aberrations. Figure 3.9a and 3.9b illustrate the chamfers applied in the water-drop lens. A full-wave simulation of the mentioned structure was done in CST, where the lens was feeded exciting the TEM mode in a discrete port and their edge had a chamfer with a fixed extension of x_0 = 0.28 mm found before. Figure 3.9c shows the reflection coefficient for different extensions of the inner chamfer x_1 and Figure 3.9d plots the maximum value of the $|S_{11}|$ within the working frequency band. It can be clearly seen that, as it happened with the chamfer in the antenna edge, there is an optimal inner chamfer length x_1 = 0.57 mm that keeps the $|S_{11}|$ below -23 dB within all the frequency band.

The resultant water-drop lens profile, in red in Figure 3.8, has an overall height taking into account the chamfers equal to h_1 = 5.5 mm. This represents a height reduction of 34.7% with respect to the geodesic lens without reflective mirroring, which measured h_0 = 8.42 mm.

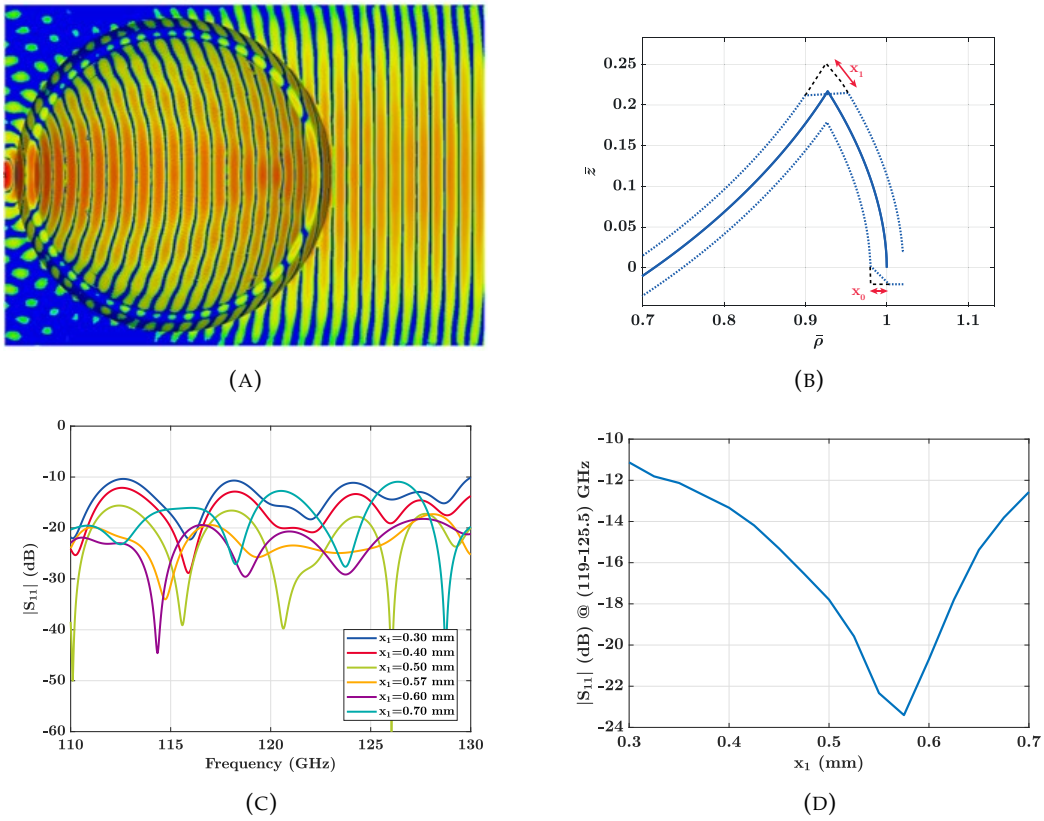

FIGURE 3.9: (A) Simulated electric field through the focusing waterdrop lens with asymmetrical chamfers. (B) Lens profile with chamfered transitions. (C) Reflection coefficient for different x_1 with x_0 = 0.28 mm. (D) Maximum value of the $|S_{11}|$ within the working frequency band in function of x_1 with x_0 = 0.28 mm.

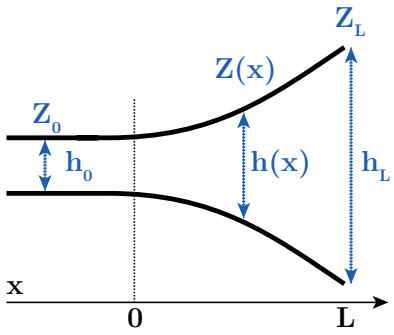

FIGURE 3.10: Tapered transmission line matching section.

3.2 Radiating Flare

The flare or taper is the element in a microwave device whose functionality is matching impedances. In the case of a lens antenna, the taper will match the impedance inside the PPW to the free space one $\eta \approx 120\ \pi$ so the energy can be efficiently radiated as illustrated in Figure 3.10.

Theory of tapered transmission lines can be read in [16], where the relation between the characteristic impedance of the taper Z and the overall reflection coefficient Γ is defined as:

$$\Gamma = \frac{1}{2}\int_{x=0}^{L} e^{-2j\beta x}\frac{d}{dx}\ln\left(\frac{Z}{Z_0}\right)dx \tag{3.6}$$

Where L is the taper length and $\beta = 2\pi/\lambda$ the propagation constant.

By changing the type of taper profile one can obtain different pass-band characteristics. In this work, we will focus on the well-known exponential flare and a small variation of it using splines.

The impedance profile of an exponential flare varies exponentially for $0 < x <$ L:

$$Z(x) = Z_0\, e^{\alpha x} \tag{3.7}$$

Where α can be found imposing $Z(0) = Z_0$ and $Z(L) = Z_L$ in Eq. 3.7:

$$\alpha = \frac{1}{L}\ln\left(\frac{Z_L}{Z_0}\right) \tag{3.8}$$

Then substituting Eq. 3.7 and 3.8 to 3.6 and assuming that β do not vary with x:

$$\Gamma = \frac{\ln\left(Z_L/Z_0\right)}{2}e^{-j\beta L}\frac{\sin\left(\beta L\right)}{\beta L} \tag{3.9}$$

Which is a sinc-shape function with the first theoretical null at $\beta L = \pi$.

Since the flare has to be used to radiate the energy, it is clear that $Z_L = \eta \approx 120\ \pi$. For finding Z_0, however, it is not trivial. The characteristic impedance for a PPW transmission line where TEM mode is propagated is:

$$Z_{PPW} = \eta \frac{h_{PPW}}{W_{PPW}} \tag{3.10}$$

Being h_{PPW} the distance between plates and W_{PPW} the width of the transmission line. In the case of a lens, the propagation is done through a circular PPW structure so the previous equation cannot be applied since the width of the structure is varying. A 3D model of the radiating exponential flare has been simulated for different aperture sizes h_L and different taper lengths L to check for the optimal dimensions that minimize Γ. And the same has been done with a variation of the exponential flare using a spline. With the spline the continuity of the plate shape derivative is guaranteed, making the transition smoother and avoiding sharp edges where the signal can be scattered.

It has been seen that a taper with a length larger than the $L = \lambda/2$ computed in Eq. 3.9 was needed to minimize the reflections. This difference is mainly due to the fact that not all the rays go through the flare with a normal incidence. Some of the rays have an oblique incidence to the flare and will follow a non-exponential aperture that may be sub-optimal.

For the design of the focusing lens, the spline flare with an aperture of h_L = 4.4 mm with an extension of $L = 1.1\lambda$, which gave a $|S_{11}|$ below -32 dB in all the frequency band.

Artificially Soft Surface

The thin profile of the lens, especially after applying one reflective symmetry, constraints the maximum antenna aperture in the E plane. This small aperture yields to a wide beamwidth in that plane that can be improved by preventing the propagation of a surface wave through the antenna profile. This can be achieved using a soft surface.

The name of soft surface (and his counterpart hard surface) comes from acoustics where porous or soft surface materials such as textiles contribute to sound absorption and hard surfaces like glass or concrete reflect sound and thus create echoes.

This behaviour can be emulated in electromagnetic signals by creating an artificial material or meta-material with the desired properties in a specific band. They are usually made by periodic structures with periodicity much smaller than the wavelength that behaves as a homogeneous material. A soft surface can be created using transversal corrugations in the lens profile as shown in Figure 3.11a.

The corrugations have to be narrow and with a period $p < \lambda/2$ so only one non-evanescent mode is present within the corrugation [11]. This is a TE_n mode with an E_l component only. Then the depth of the corrugation d is chosen so at the top of the surface:

$$Z_l = -\frac{E_l}{H_t} = \infty \tag{3.11}$$

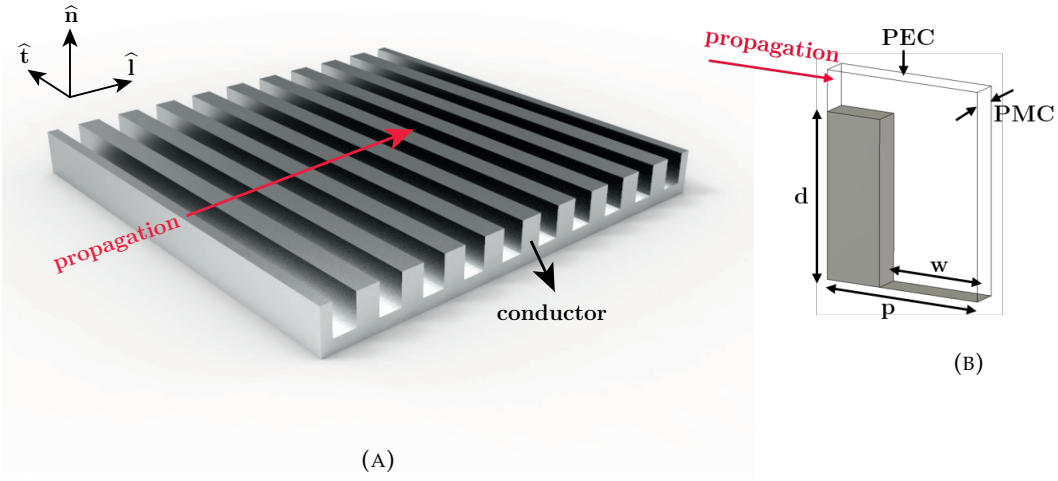

FIGURE 3.11: (A) Soft surface using corrugations. (B) Unit cell of a corrugated periodic structure.

$$Z_t = \frac{E_t}{H_l} = 0 \tag{3.12}$$

For a planar wave that is incident to a corrugated surface like the one shown in Figure 3.11a, the depth of the corrugations must be $d = \lambda/4$ in order to fulfil Eq. 3.11 and 3.12.

The periodic structure can be analyzed using the CST eigenmode solver and simulating the corrugation unit cell illustrated in 3.11b. The results obtained are shown in Figure 3.12 in a dispersion diagram for different gaps w. The dispersion diagram describes the effect of dispersion on the properties of waves in a medium and it relates the wavelength or wavenumber of a wave to its frequency.

In Figure 3.12 the unit cell periodicity and depth to $p = d = \lambda/4 \approx 0.62$ mm has been set. It can be seen that the fundamental mode does not propagate at our frequency band, marked in black-dashed lines in the figure. Furthermore, it can be noticed that for wider corrugations gaps the mode stops propagating at smaller frequencies.

The soft surface has been added to the antenna profile next to the radiating flare ending. The simulated far field radiation diagram with a simplified straight profile as it is shown in Figure 3.13a 3.13b, where the corrugated surface is compared with the non-corrugated one. The effect of the corrugations is clear when looking at the antenna directivity at 90º from the maximum, which is the direction that the corrugations block the propagation of a plane wave. Furthermore, with the corrugations, the back radiation is significantly decreased. This can be due to the fact that the energy that reaches the structure edge has already been attenuated by the metasurface, decreasing the power of the signal scattered in the edge. In practice, there is no gain in having more than two corrugations since the remaining signal after going through them is almost negligible.

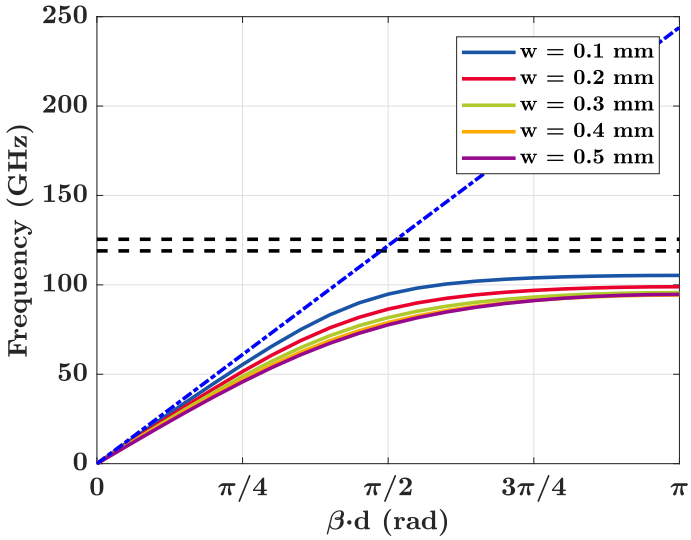

FIGURE 3.12: Dispersion diagram of the corrugation unit cell with d=p=$\lambda/4$. The line-of-light is shown in dashed blue.

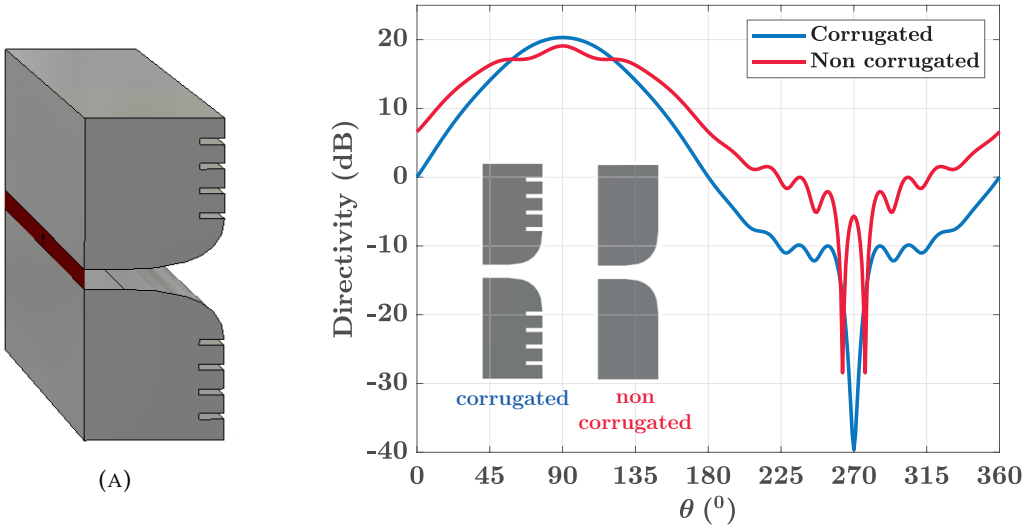

(A)

(B)

FIGURE 3.13: (A) Model of a straight spline flare excited with a TEM mode. (B) Radiation pattern of a corrugated and non-corrugated infinite straight spline flare.

3.3 Component Integration

The focusing lens will be fed through an external COTS transceiver. The chip used contains a transmitter and receiver antenna inside the chip itself so a small aperture antenna has been used to gather the radiated energy from the chip and confine it to the lens. Both the chip and the proposed lens feeder section are described in the next subsections.

Chip

The chip used is the TRA-120-002 [1] from SILICON RADAR, which is a compact radar front-end integrated on a chip that works at the 120 GHz ISM band.

Since it is a FMCW radar, the system works with two separated antennas for the transmitter and receiver chain respectively. In the case of the TRA-120-002 chip the antennas, that are integrated into the IC are seen in Figure 3.14a. The antennas are highly coupled, as it can be shown in the simulated radiation pattern provided in the component datasheet and attached in Figure 3.14b, where the main lobe has a magnitude of 10 dB and tilted around 30º. This directivity using a dipole can only be achieved by constructive interference with the signal reflected in the chip ground plane and coupled to the other antenna, working as a passive driven element in a similar way that the Yagi-Uda working principle.

No more information regarding the chip RF model was provided by the manufacturer so a model in CST was built so it replicates the available far-field behaviour. The model in Figure 3.15a has a simulated radiation pattern (Figure 3.15b) close to the one provided by the component datasheet. It is important to notice that the results were achieved assuming an infinite ground plane in the chip base. This assumption can be accurate if the chip is soldered in a PCB with a top ground plane.

The main application of the radar front end is in short-range radar systems with a range up to about 10 meters. The manufacturer claims that the range can be increased if a dielectric lens is used. The use of those lenses at mmW band, however, yield an important attenuation of the signal in the dielectric as explained in section 1.2.1. Moreover, one characteristic of those lenses is that they transform the rays coming from a single source point to a collimated beam with minimal dispersion. Due to the double antenna design of the system, each of the antennas will have an offset of 1.67/2 mm with respect to the lens focal axis, causing a tilt in the main beam and aberrations due to the out of focus position of the antennas. This phenomenon is represented in Figure 3.16a, where the beam tilt effect is accentuated since the offset of the receiver and transmitter antenna cause opposite tilts in the respective radiation beams. This behaviour is simulated in Figure 3.16b, where a dielectric hyperbolic lens has been fed from a point shifted 1.67/2 mm with respect to the lens focal axis. In that figure, the tilt of the main beam can be clearly seen. Also one can notice that the wave being radiated is not completely planar due to the aberrations, mainly comatic in this case.

Lens Feeder

Due to this high non-symmetries in the radiation pattern of the chip, together with the lack of near-field information, a special aperture to confine the fields before feeding the lens was designed. This was found to be necessary for having all the fields

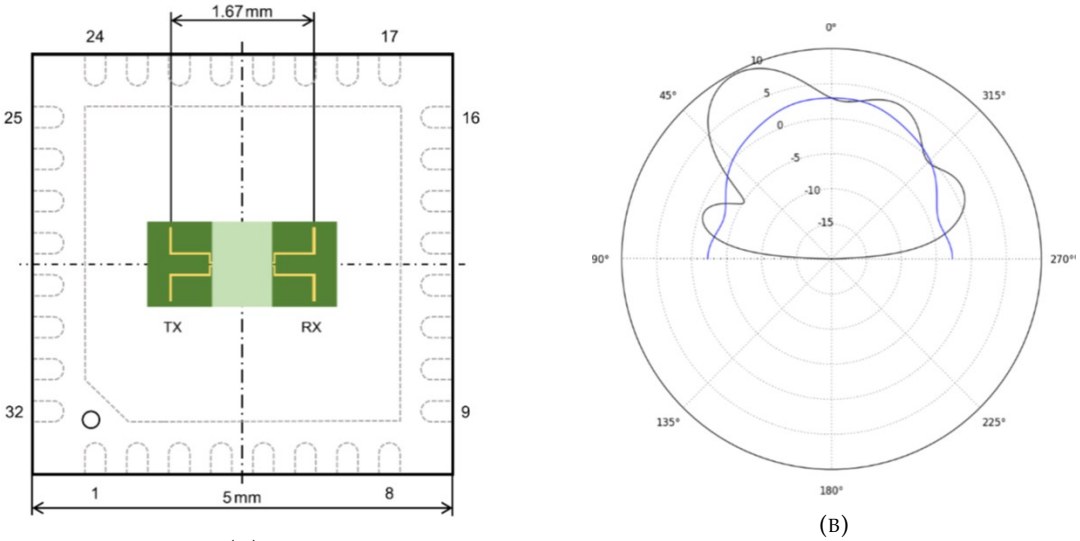

(A) (B)

FIGURE 3.14: (A) Antennas integrated in the TRA-120-002 chip. Image yielded from [1]. (B) Radiation pattern provided by the manufacturer.

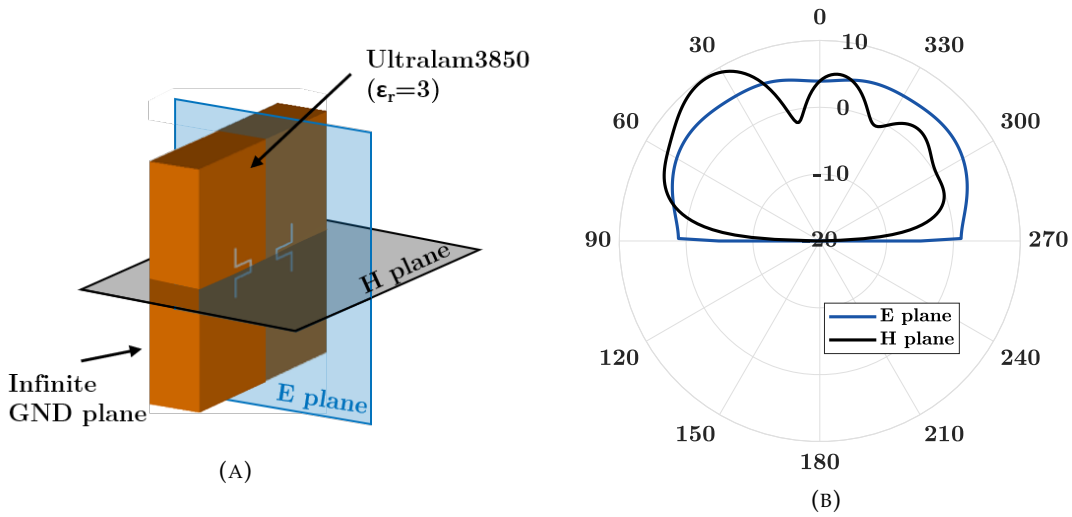

(A) (B)

FIGURE 3.15: (A) Simulated model in CST. (B) Radiation pattern of the simulated model.

with a common and single-phase origin before going through the lens, otherwise the resulting wave exiting the lens was far from being planar.

The proposed solution consists of a rectangular horn that gathers as much energy as possible from the one radiated by the chip and confines it to a rectangular waveguide. The waveguide interfaces with the lens PPW so the height is constrained by the distance between plates $h_w = h = 0.5$ mm, as found in Eq.3.3. The width of the waveguide has been chosen so only the fundamental mode TE_{10} can be propagated.

The cut-off frequency of a rectangular waveguide is:

$$f_c = \frac{1}{2\sqrt{\mu\epsilon}}\sqrt{\left(\frac{n}{h_w}\right)^2 + \left(\frac{m}{w_w}\right)^2} \tag{3.13}$$

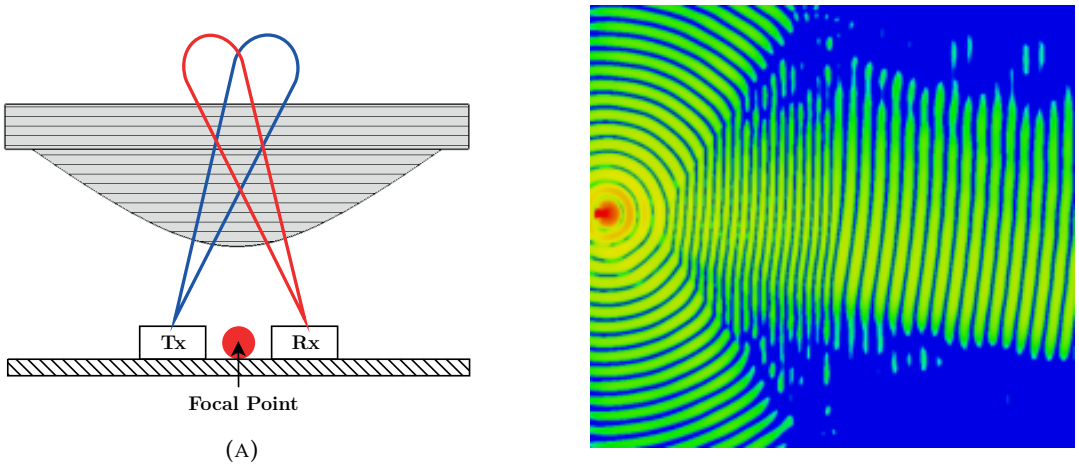

(A) (B)

FIGURE 3.16: (A) Illustration of a transceiver with independent transmitter and receiver antennas feeding the same dielectric lens. (B) CST simulation of an hyperbolic dielectric lens with a source point shifted from the lens focal axis.

So in order to propagate the TE_{10} ($m = 1$, $n = 0$):

$$w_w > \frac{c}{2 \cdot 119x10^9} = 1.26mm \tag{3.14}$$

And for avoiding the propagation of the TE_{20}:

$$w_w < \frac{c}{225.5x10^9} = 2.39mm \tag{3.15}$$

A safe width of w_w = 2 mm has been chosen for the design of the transition.

The model of Figure 3.15a has been used to find the optimal aperture of the lens feeder and the best spacing from the chip. The transmission between one of the chip antennas to the waveguide output has been simulated adapting the remaining chip antenna. The best performance was achieved with an aperture of a = 2.6 mm x b = 2.15 mm, placing the chip as close as possible to the aperture. In Figure 3.17 it can be seen that the overall transmission obtained with this solution is poor being around -6.5 dB within the working band but the best achieved without modifying the COTS component. This response was almost unaffected by the change of the feeder horn length L. For a better integration with the lens, the horn length has been set to L = 1.1 λ, which is the same extension than the radiating flare.

From the simulations, it has been seen that a big amount of energy was confined in the chip dielectric and a TEM mode was excited between the PCB where the chip was placed and the profile of the lens feeder. This energy loss not only decreased the overall gain but was radiated increasing the SLL.

An Electromagnetic Band-Gap (EBG) structure was used to decrease the mentioned spillover, which is a structure that creates a stopband to block electromagnetic waves of certain frequency bands. This can be achieved using meta-surfaces making use of periodic structures. In that case the well known Fakir´s bed of nails metamaterial, which can be seen as a 2D implementation of the artificial soft surface used in the radiating flare.

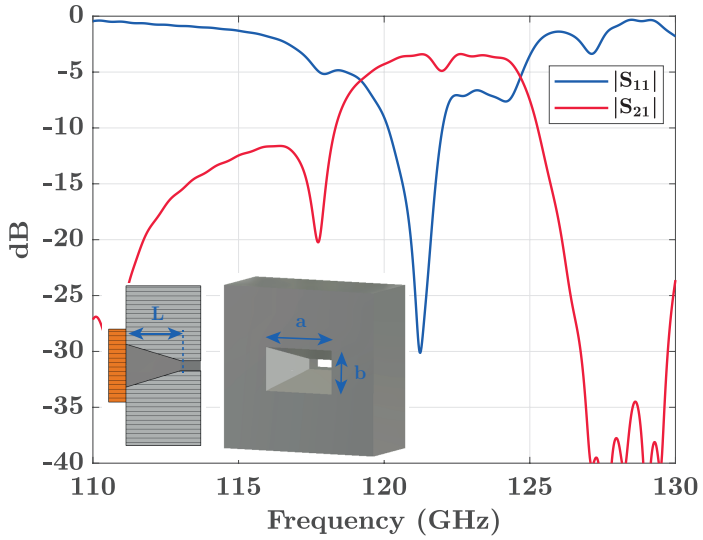

FIGURE 3.17: S-parameters of the chip and feeder horn combination.

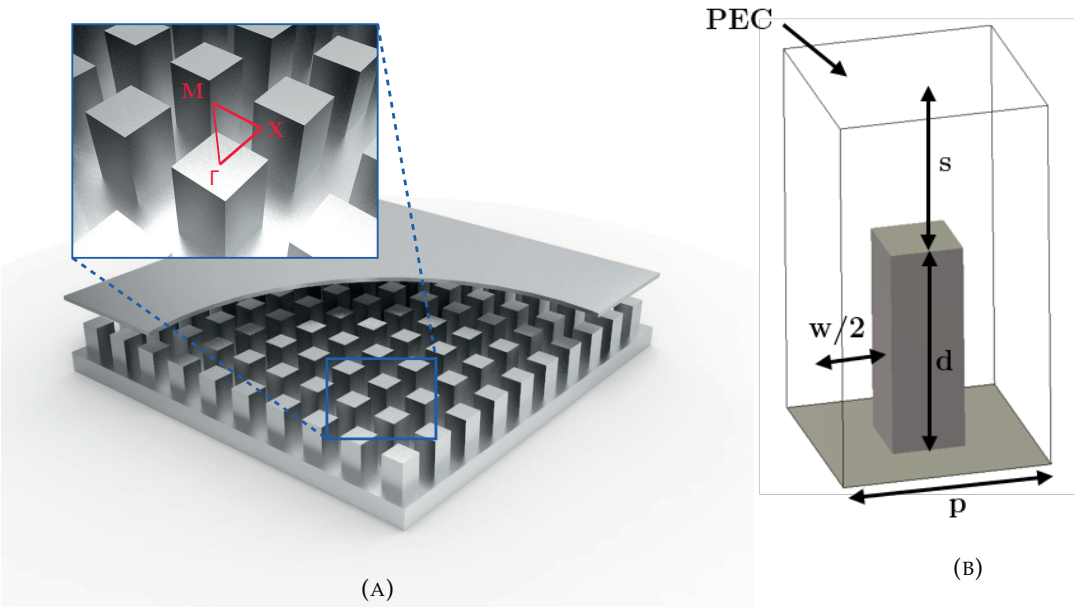

(A) (B)

FIGURE 3.18: (A) Fakir bed of nails metasurface. (B) Unit cell of a bed of nails periodic structure.

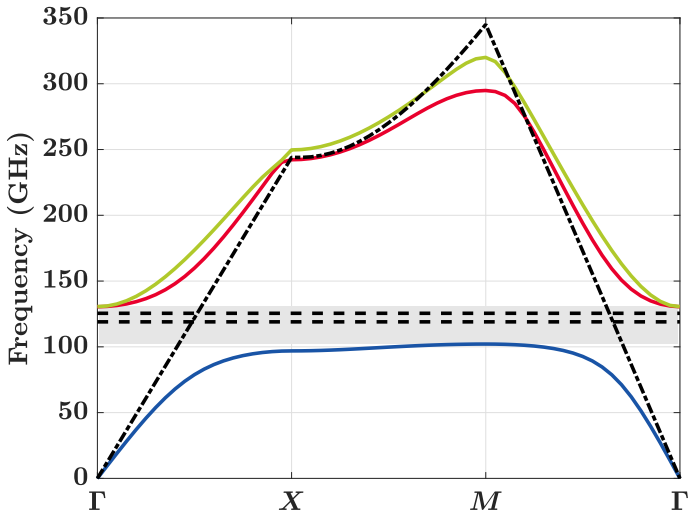

FIGURE 3.19: Dispersion diagram of the bed of nails unit cell with d=p=$\lambda/4$. The line-of-light is shown in dashed black.

Figure 3.18b illustrates the unit cell used, with a periodicity and nail depth equal to $p = d = \lambda/4$, a gap between nails $w = 0.4$ mm and a separation between the nails and the top plate $s = 0.5$ mm. This value of s will be the maximum distance between the PCB where the chip is soldered and the bed of nails so a stop-band can be created.

Now we can have waves propagating in any direction β_x and β_y the study of the Brillouin zone has to be done. The Brillouin zone is a uniquely defined primitive cell in reciprocal space that for a squared lattice like the bed of nails it is defined by the triangle $\Gamma XM\Gamma$. The resulting dispersion diagram shown in Figure 3.19 was obtained using the CST eigenmode solver where the three first modes are plotted with continuous lines. A stop-band (gray region) between 102 GHz to 130 GHz was obtained for the dimensions mentioned above.

Finally a simulation of the lens feeder with the metasurface together with the chip has been done. Only two rows of nails where used due to size constraints as seen in Figure 3.20, showing in Figure 3.21 an improvement in the amount of energy transmitted to the waveguide in most of the band and decreasing the spillover significantly.

3.4 Mechanical implementation

Once the geodesic shape, flare and feeder has been studied all the parts were put together. In chapter 4 the final geometries and results are presented. However, some modifications had to be done in the structure in order to overcome possible problems due to manufacturing limitations, especially at mmW band were tolerances are critical.

3.4.1 Effect of a gap between pieces

The fully metallic geodesic lenses are usually manufactured in two pieces by milling. These two pieces are separated $h = 0.5$ mm among the geodesic shape and flare in order to create a PPW and allow the TEM mode to propagate within them. The

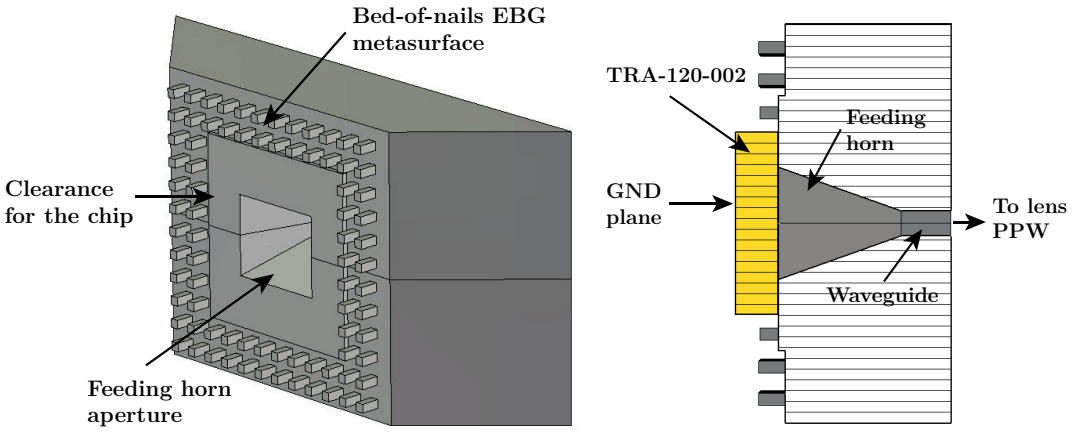

FIGURE 3.20: Lens feeder 3D model and its respective profile.

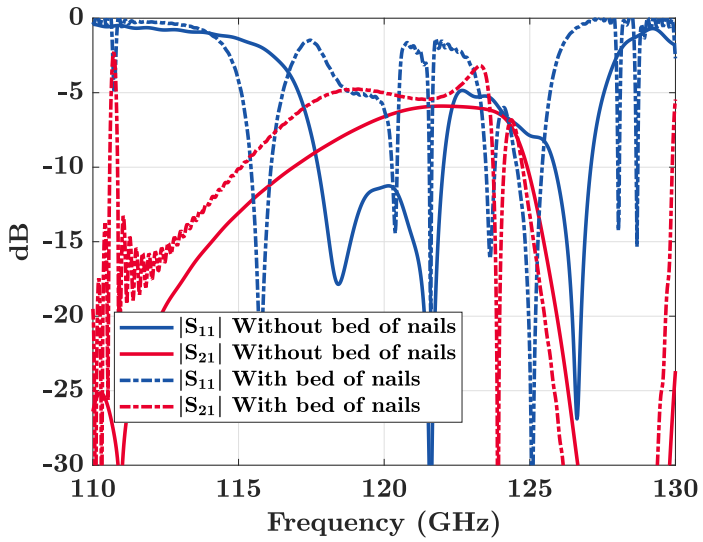

FIGURE 3.21: S parameters of the chip and horn feeder combination with and without the use of a bed-of-nails metasurface.

FIGURE 3.22: Lens profile with a gap between both plates.

two pieces, however, must be in contact with the feeder structure for two reasons. The first one is that in the horn feeder we want to confine the fields radiated by the FMCW radar chip to a waveguide. Any gap in the horn or waveguide sides will cause a big amount of leakage, decreasing the power delivered to the lens but also feeding the lens in undesired points causing an increase of the SLL. The second reason is purely mechanical: The two pieces of the lens must be fixed to guarantee a specific distance between plates. Since the wave propagates in air in order to avoid dielectric losses, we need a point of contact between the two lens pieces so we can screw both of them together.

At mmW band the manufacturing tolerances together with a non-perfect surface finish can easily deteriorate the performance of the lens. Several simulations with different uniform gaps as illustrated in Figure 3.22 were done to check this effect. In practice, the gap will never be uniform but with varying size and the surface roughness will help to attenuate the signal leakage. In Figure 3.23 we can clearly see the effect of that gap in the dispersion diagram of the lens antenna. The results, summarized in Table 3.2 show a clear increase in SLL for different uniform gaps and a deterioration in the antenna directivity.

Parameter	**gap = 0 μm**	**gap = 20 μm**	**gap = 30 μm**
Directivity	18.8 dBi	17 dBi	14.3 dBi
SLL (wrt. D_{max})	-13.9 dB	-6.7 dB	0.8 dB
F/B (wrt. D_{max})	-20.5 dB	-20.3 dB	-30.7 dB

TABLE 3.2: Effects of a gap between the antenna plates in the antenna performance at 122 GHz.

In order to prevent the leakage, an EBG metasurface was placed between the two metallic antenna pieces. In that case a variation of the glide-symmetric holey metasurface [9] was used. With this structure, a big stop-band can be achieved at 122 GHz using a unit cell periodicity much larger than the pins, reducing the required accuracy and cost for manufacturing at high frequencies. The unit cell is shown in Figure 3.24 and its respective dispersion diagram in Figure 3.25, where a stop-band from 100 GHz to 148 GHz between the 2^{nd} and 3^{rd} modes is achieved and marked in gray in the Figure.

Figure 3.26 compares the effect of a uniform 20 μm gap in the lens feeder for different structures. As shown before, if nothing is done to prevent the signal to leak, there is a noticeable part of the energy that propagates within the lab. When implementing the holey 2D glide-symmetric periodic structure designed before, there is an improvement but not enough to prevent the leakage. This is due to the limited space in the feeder, where only one row of few holes could fit. A much better result was obtained by shifting all the holes near to the horn, waveguide and PPW

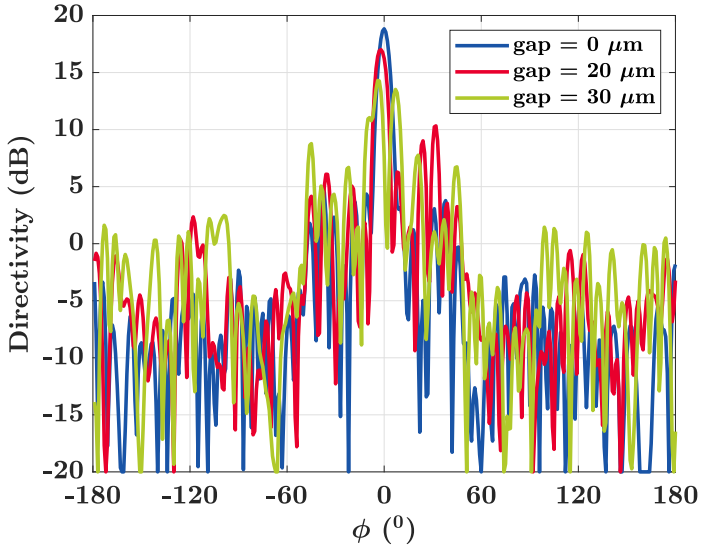

FIGURE 3.23: Radiation pattern in function of the gap between pieces.

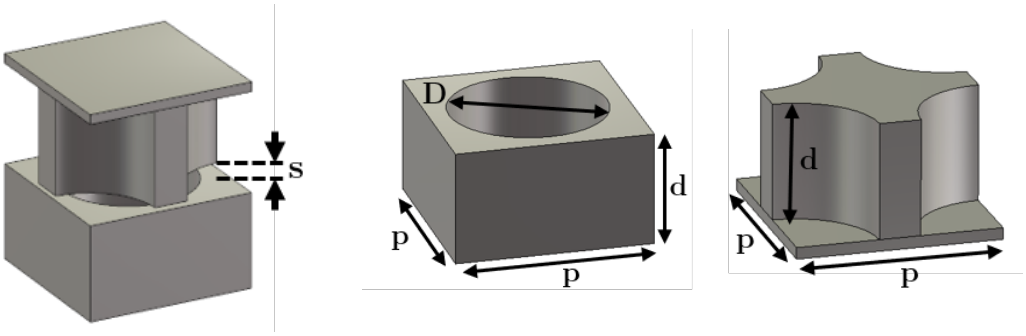

FIGURE 3.24: Unit cell of the holey glide-symmetric periodic structure.

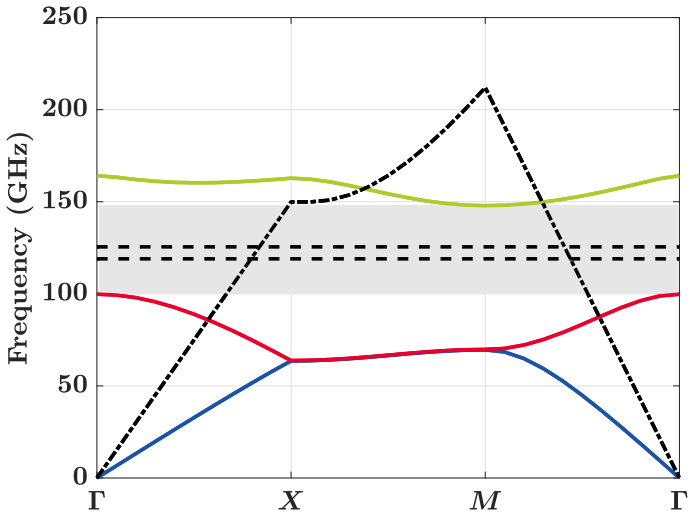

FIGURE 3.25: Dispersion diagram of the glide-symmetric hole unit cell with p = 1 mm, D = 1.4 mm, d = 0.5 mm and s = 0.05 mm. The line-of-light is shown in dashed black.

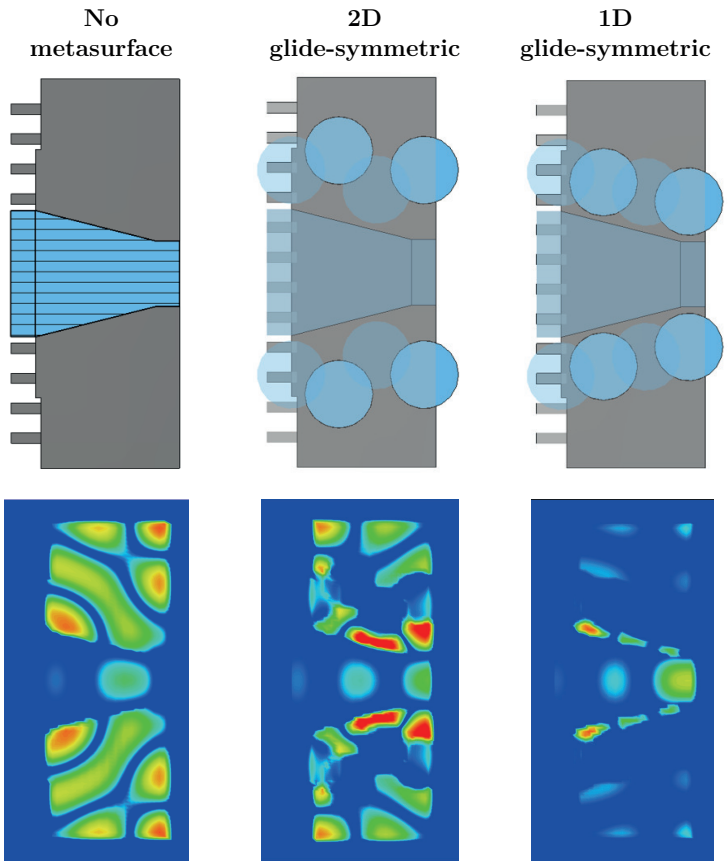

FIGURE 3.26: Simulation of the feeder electric field leaked inside a 20 μm gap for different structures.

which almost completely block any kind of propagation within the gap. This last approach, called 1D glide-symmetric in this report, was the one being used in the designed focusing lens.

The radiation pattern for different undesired gaps between the lens pieces has been resimulated using the 1D offset holey metasurface. Figure 3.27 compares the radiation pattern obtained when the gap between antenna plates is increased. Table 3.3 summarizes the results. It can be seen that both the directivity and SLL get worse when the gap is increased but the values achieved are much better than without using the EBG metasurface.

Parameter	**gap = 0 μm**	**gap = 20 μm**	**gap = 30 μm**
Directivity	18.9 dBi	17.9 dBi	17.2 dBi
SLL (wrt. D_{max})	-14.2 dB	-10.33 dB	-7.54 dB
F/B (wrt. D_{max})	-22.1 dB	-29.2 dB	-22.6 dB

TABLE 3.3: Effects of a gap between the antenna plates in the antenna performance at 122 GHz when holey glide-symmetric periodic structure is used.

Screws

In order to keep both plates guaranteeing a distance between them of h = 0.5 mm they have to be screwed in the feeder structure, since is the only part of the lens

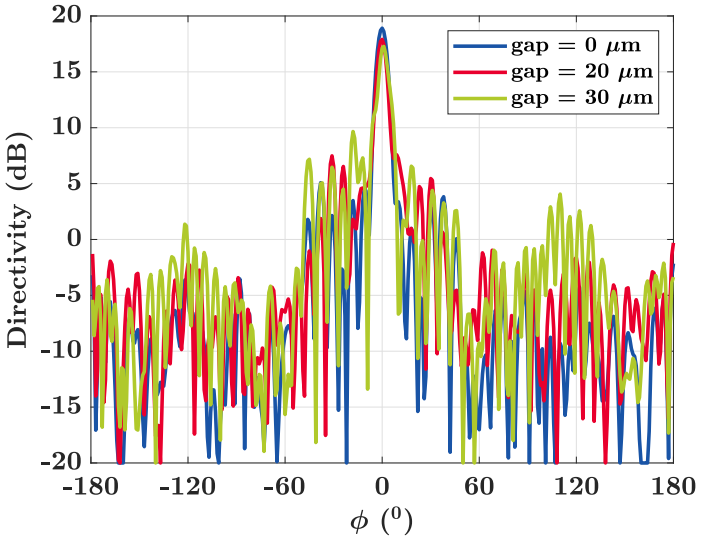

FIGURE 3.27: Radiation pattern in function of the gap between pieces using a holey EBG mestasurface.

where both plates are in contact.

Four standard screws of metric M1 will be used in this prototype to tightening both lens parts. The top plate is designed with holes that go through all the structure and then threaded holes are done in the bottom layer. In Appendix A sketches of both plates can be found with all the mechanical requirements and tolerances, where the external shape of the feeder had to be slightly increased in order to fit the screws.

The plates have two extra threaded holes of metric M1.6 in each surface for screwing the lens to a supporting structure. A PLA supporting structure has been designed and manufactured to maintain the lens just on the top of the TRA-120-002 transceiver and interface with the evaluation board *SiRad Easy* from SILICON RADAR. Plastic material has been chosen to not interfere with the lens and the radiating flare was kept free of obstacles for the same reason. Appendix A includes also an image of the support.

Chapter 4

Results

After studying all the parts of the lens separately, the final antenna has been assembled interfacing the different segments and taking into account the considerations of section 3.4. The resulting antenna geometry is shown in Figure 4.1, which is composed of two independent metallic plates for facilitating its manufacturing. Figure 4.2 shows a schematic of the lens profile which provides a better understanding of the rays path. In that figure, all the stages can be clearly differentiated.

The overall antenna fits inside a cylinder with 31.45 mm of diameter and 8 mm height which is only around 35% bigger in diameter than 1€ coin. Furthermore, it is important to notice that the lens has a diameter of 25.1 mm including the gap between plates in the PPW. This represents almost 80% of the antenna size, meaning that the available space is being used efficiently.

FIGURE 4.1: Rendering of the resulting top and bottom plates models.

In order to check the overall performance, a full-wave simulation was done. The transceiver model designed in section 3.3 was used together with a small ground plane emulating the PCB where the chip will be placed. The existence of the PCB plays an important role in allowing to create an EBG structure together with the bed-of-nails periodic structure already integrated in the lens, as designed in the mentioned section. Due to the transceiver and the lens antenna symmetries, only one of the chip dipoles was excited for computing the far-fields. Exciting the lens through the other chip antenna will lead to symmetric results.

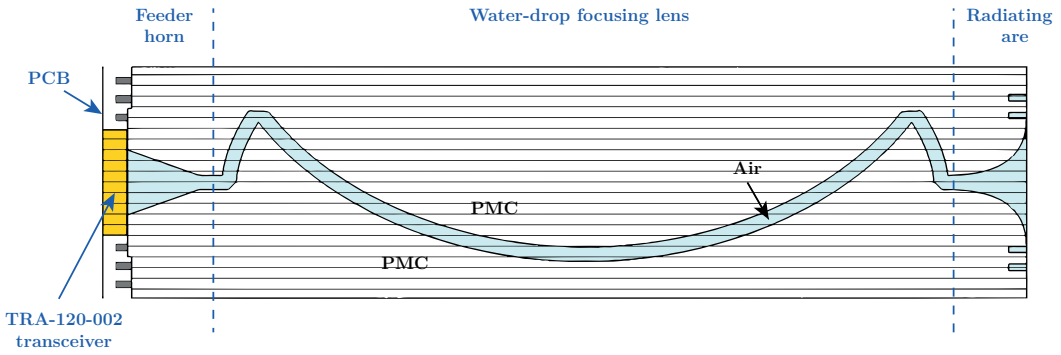

FIGURE 4.2: Antenna profile.

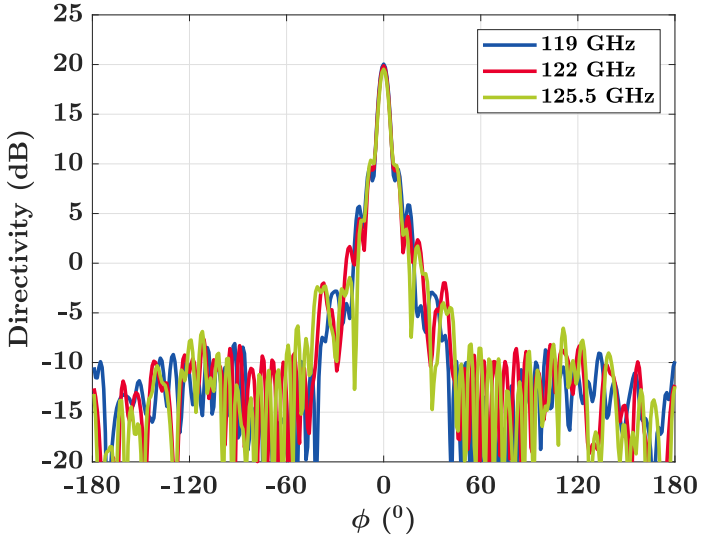

FIGURE 4.3: Simulated H-plane radiation diagram of the overall transceiver and lens antenna.

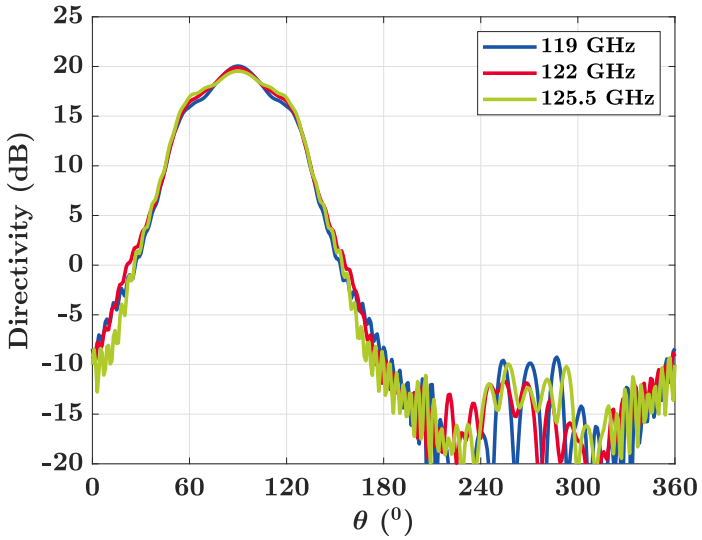

FIGURE 4.4: Simulated E-plane radiation diagram of the overall transceiver and lens antenna.

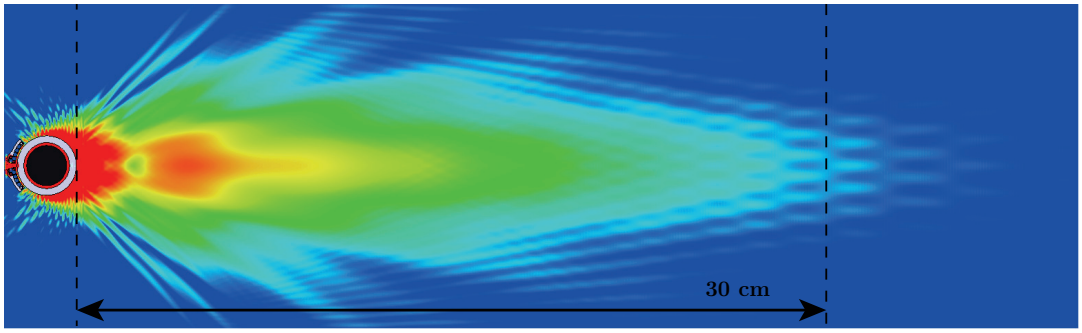

FIGURE 4.5: Simulation of the electric field magnitude at 30 cm from the lens.

The energy transmitted by the transceiver, gathered by the lens antenna and re-radiated was simulated giving the H-plane and E-plane radiation pattern for the overall structure and shown in Figure 4.3 and 4.4 respectively. From both figures it can be seen that the radiation pattern remains almost constant between all the working band of the FMCWradar (119 GHz - 125.5 GHz) where the difference in the main beam directivity is < 0.6 dB and the difference in the 3 dB bandwidth < 0.2^{o} in the H-plane. This characteristic is very important for performing proper imaging radar readings.

A directivity > 19.5 dB is achieved in all the band with SLL between -10.5 dB and -9.2 dB. Since the design of a focusing lens has been done, high directivity should not be a factor of quality since the lens differs from Luneburg's one. Nevertheless, as seen in section 3.1, for the specific antenna dimensions and focusing distance the resulting focusing lens is very close to one that radiates a collimated beam. For this reason, high directivities are expected.

Finally, Figure 4.5 shows the magnitude of the electric field at long distances. The antenna was designed to have a focal point at 30 cm from the lens or equivalently 122 $\lambda \approx$ 12R being R the lens radius. This can be checked by seeing the phase front shape and field magnitudes. However, as already said and seen in Figure 3.2 at these focusing distances the phase front was already almost planar at the lens output.

Chapter 5

Conclusions and Future Work

5.1 Conclusions

In this work an alternative to the dielectric Luneburg lens antennas used for enhancing the directivity of mmW radar COTS transceivers have been studied for the specific case of radar imaging, where the lens focusing properties are interesting.

The proposed solution is a fully metallic focusing geodesic lens with a water-drop shape to decrease the antenna profile. With this solution, an improvement in the overall losses is expected since no dielectric materials are used. Furthermore, the antenna is specifically designed for 30 cm imaging purposes, so a slight improvement in the resolution can be achieved by properly shaping the lens.

The design of the focusing antenna has been done by parts, so each one of the sections involved has been properly optimized before integrating all of them. The designed lens antenna can be split in three main sections: a focusing lens, a radiating flare and a feeder.

The lens shape was successfully generated using transformation optics for a 30 cm imaging point and its height has been decreased a 34.7% applying one reflective mirroring. A special study has been done in all of the shape non-linearities where asymmetrical chamfers were selected among other solutions since low reflections could be achieved without modifying the lens shape and increasing the aberrations. $|S_{11}|$ below -23 dB were achieved within all the band.

For matching the PPW impedance to the free-space one, a variation of the exponential flare using splines was used in order to avoid sharp edges where the signal could scatter. A resulting flare of length 2.7 mm (1.1 λ) and an aperture of 4.4 mm (smaller than the lens height) gave $|S_{11}|$ below -32 dB. Corrugations were then added to the lens profile improving the E-plane radiation pattern.

The best solution found to interface the COTS transceiver with the lens antenna was through a 2.6 mm x 2.15 mm horn aperture of length 2.7 mm (1.1 λ) that confines the field radiated by the chip to a waveguide before feeding the lens antenna. This solution gave insertion loses of around 6 dB after implementing a bed-of-nails EBG around the transceiver for preventing the signal to leak. Despite all the efforts, there is room for improvement in the feeder part, which is the limiting part of the overall lens antenna.

A study of some of the effects of the manufacturing limitations has been done, especially an undesired gap between plates was foreseen, where a critical deterioration of the radiating pattern was expected. A variation of the holey glide-symmetric EBG

metasurface was added between the plates successfully decreasing the signal leakage in the presence of a gap.

5.2 Future Work

One of the main properties of interest of the lenses are the beamforming capabilities due to its rotational symmetry. In this work, only one feeder was contemplated but multiple feeding apertures can be integrated into the antenna lens and support the feeding from multiple transceivers.

Moreover, as mentioned in the final conclusions, the interface between the antenna feeding and the transceiver is limiting the overall performance. This is due to the difficulties of interface with an unknown source with heavily coupled antennas. A more efficient way to transfer the energy from the chip to the lens antenna can be done if both components are designed accordingly.

Finally, the manufacturing of a prototype has to be done for understanding the mechanical limitations and the effect of the materials and surface finish at mmW frequency band.

Chapter 6

Ethics and Sustainability

This project has the main goal to overcome one existing problem in radar imaging at mmW band so has no direct impact on any ethical problem. The applications of imaging at those frequencies can be extremely diverse like security scans, material characterization, autonomous drive, etc. Some of the applications can present ethical issues but due to the application and not due to the technology used or antenna in this case.

Regarding the sustainability effects of this project, there are no other effects than possible pollution during its manufacturing process. The lens antenna is fully metallic and can be built by milling. Since the working frequency is 122 GHz, the overall size of the antenna is slightly higher than 1€ coin so the material waste is very limited. On the other hand, really high resolutions are needed, yielding to an increase in their manufacturing time. This manufacturing time increase can be understood as a higher energy waste in all the machines involved.

Bibliography

[1] *120 GHz Transceiver TRA_120_002 - Silicon Radar GmbH*. URL: https://siliconradar.com/products/single-product/120-ghz-transceiver-tra_120_002/.

[2] George B Arfken, Hans J Weber, and Donald Spector. "Mathematical Methods for Physicists, 4th ed". In: *Mathematical Methods for Physics and Engineering American Journal of Physics* 67.2 (Feb. 1999), p. 461. DOI: 10.1119/1.19217. URL: https://doi.org/10.1119/1.19218.

[3] R. Bamler. "Principles of synthetic aperture radar". In: *Surveys in Geophysics* 21.2-3 (2000), pp. 147–157. ISSN: 01693298. DOI: 10.1023/A:1006790026612. URL: https://link.springer.com/article/10.1023/A:1006790026612.

[4] Pilar Castillo-Tapia et al. "Modulated Geodesic Lens Antenna Array". In: *15th European Conference on Antennas and Propagation, EuCAP 2021*. Institute of Electrical and Electronics Engineers Inc., Mar. 2021. ISBN: 9788831299022. DOI: 10.23919/EuCAP51087.2021.9411158.

[5] JC Curlander and RN McDonough. "Synthetic aperture radar". In: *Wiley, New York* 11 (1991). URL: https://www.academia.edu/download/47829925/handout1.pdf.

[6] J. E. Eaton. "On spherically symmetric lenses". In: *Transactions of the IRE Professional Group on Antennas and Propagation* PGAP-4.1 (1952), pp. 66–71. ISSN: 21680647. DOI: 10.1109/TPGAP.1952.237341.

[7] Nelson J G Fonseca, Qingbi Liao, and Oscar Quevedo-Teruel. "The Water Drop Lens: a Modulated Geodesic Lens Antenna Based on Parallel Curves". In: *International Symposium on Antennas and Propagation (ISAP)*. 2018.

[8] Nelson J.G. Fonseca, Qingbi Liao, and Oscar Quevedo-Teruel. "Equivalent Planar Lens Ray-Tracing Model to Design Modulated Geodesic Lenses Using Non-Euclidean Transformation Optics". In: *IEEE Transactions on Antennas and Propagation* 68.5 (May 2020), pp. 3410–3422. ISSN: 15582221. DOI: 10.1109/TAP.2020.2963948.

[9] Fatemeh Ghasemifard et al. "Analyzing Glide-Symmetric Holey Metasurfaces Using a Generalized Floquet Theorem". In: *IEEE Access* 6 (2018), pp. 71743–71750. ISSN: 21693536. DOI: 10.1109/ACCESS.2018.2882056.

[10] *ITU-R P.676 : Attenuation by atmospheric gases and related effects*. 2019. URL: https://www.itu.int/rec/R-REC-P.676/en.

[11] Per Simon Kildal. "Artificially Soft and Hard Surfaces in Electromagnetics". In: *IEEE Transactions on Antennas and Propagation* 38.10 (1990), pp. 1537–1544. ISSN: 15582221. DOI: 10.1109/8.59765.

[12] K. S. Kunz. "Propagation of microwaves between a parallel pair of doubly curved conducting surfaces". In: *Journal of Applied Physics* 25.5 (1954), pp. 642–653. ISSN: 00218979. DOI: 10.1063/1.1721704.

[13] Q. Liao, N. J.G. Fonseca, and O. Quevedo-Teruel. "Compact Multibeam Fully Metallic Geodesic Luneburg Lens Antenna Based on Non-Euclidean Transformation Optics". In: *IEEE Transactions on Antennas and Propagation* 66.12 (Dec. 2018), pp. 7383–7388. ISSN: 0018926X. DOI: 10.1109/TAP.2018.2872766.

[14] R.K. Luneburg. *Mathematical Theory of Optics*. University of California Press, Aug. 1964. DOI: 10.1525/9780520328266.

[15] J. C. Maxwell. "Scientific Papers, I". In: *Dover Publications, New York* (1860).

[16] David M Pozar. *Microwave engineering*. Ed. by John wiley & sons. 2011.

[17] R. F. Rinehart. "Journal of Applied Physics 19". In: *Journal of Applied Physics* 19.9 (Apr. 1948), pp. 860–862. ISSN: 00218979. DOI: 10.1063/1.1698221. URL: https://doi.org/10.1063/1.1698221.

[18] Martin Šarbort and Tomáš Tyc. "Spherical media and geodesic lenses in geometrical optics". In: *Journal of Optics (United Kingdom)* 14.7 (July 2012), p. 075705. ISSN: 20408986. DOI: 10.1088/2040-8978/14/7/075705. URL: https://iopscience.iop.org/article/10.1088/2040-8978/14/7/075705https://iopscience.iop.org/article/10.1088/2040-8978/14/7/075705/meta.

[19] Van E. Wood. "Effects of edge-rounding on geodesic lenses". In: *Applied Optics* 15.11 (Nov. 1976), p. 2817. ISSN: 0003-6935. DOI: 10.1364/ao.15.002817. URL: https://www.osapublishing.org/viewmedia.cfm?uri=ao-15-11-2817&seq=0&html=truehttps://www.osapublishing.org/abstract.cfm?uri=ao-15-11-2817https://www.osapublishing.org/ao/abstract.cfm?uri=ao-15-11-2817.

Appendix A

Lens sketches

A.1 Top Plate

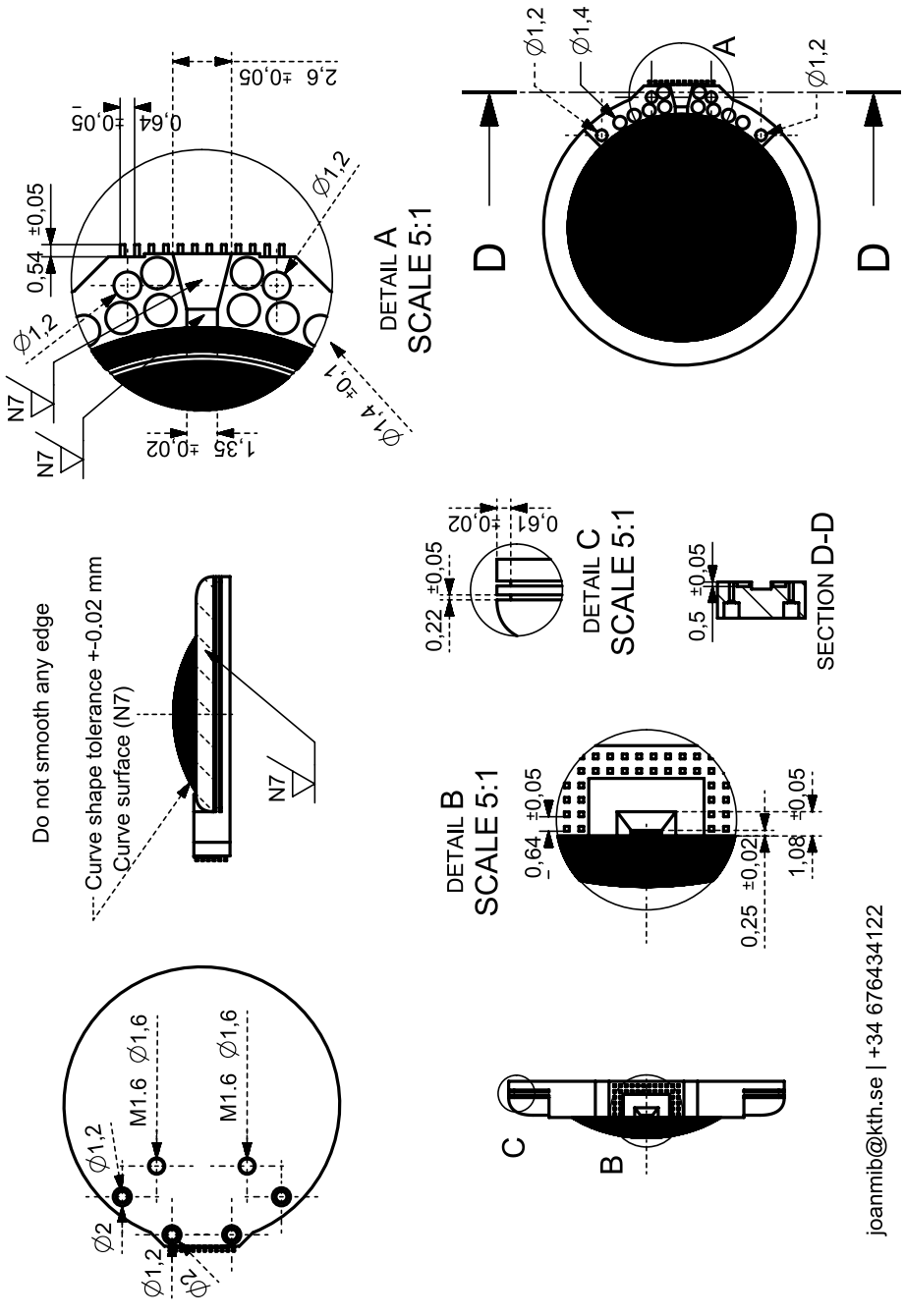

A.2 Bottom Plate

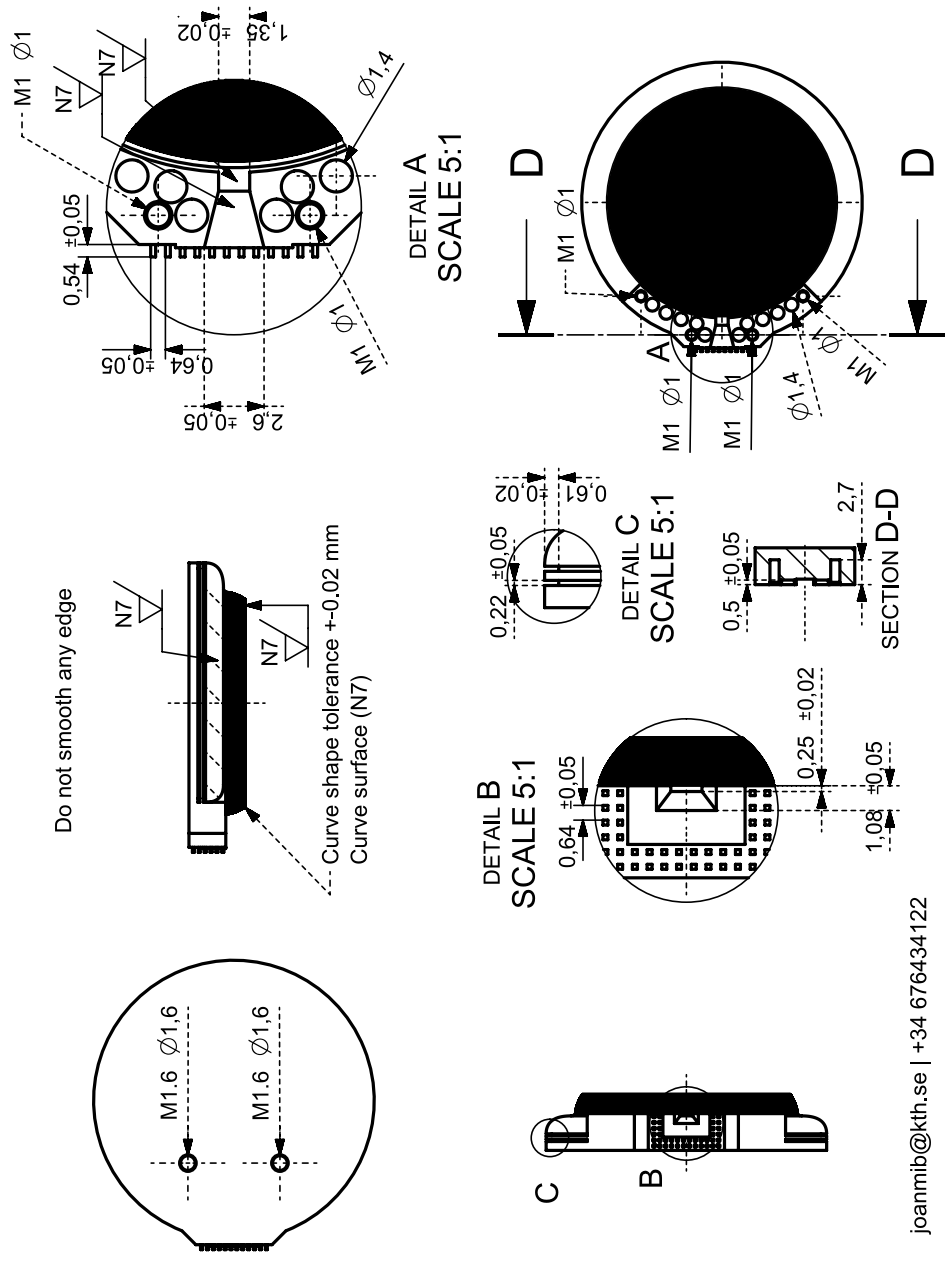

A.3 Lens Support